Applied Acoustics 240 (2025) 110876

Contents lists available at ScienceDirect

Applied Acoustics

journal homepage: www.elsevier.com/locate/apacoust

An empirical wall-pressure spectrum model for aeroacoustic predictions based on symbolic regression

Laura Botero-Bolívar [a,*], David Huergo [a], Fernanda L. dos Santos [c], Cornelis H. Venner [b], Leandro D. de Santana [d], Esteban Ferrer [a]

[a] *ETSIAE-UPM - School of Aeronautics, Universidad Politécnica de Madrid, Plaza Cardenal Cisneros 3, Madrid, 28040, Spain*
[b] *University of Twente, Drienerlolaan 5, Enschede, 7522 NB, Netherlands*
[c] *MARIN Maritime Research Institute Netherlands, Netherlands*
[d] *NLR Netherlands Aerospace Centre, Netherlands*

ARTICLE INFO

Keywords:
Aerodynamic noise
Trailing-edge noise
Wall-pressure spectrum model
Symbolic regression
Machine learning
Wall-pressure fluctuations measurements

ABSTRACT

Fast-turn around methods to predict airfoil trailing-edge noise are crucial for incorporating noise limitations into design optimization loops of several applications. Among these aeroacoustic predictive models, Amiet's theory offers the best balance between accuracy and simplicity. The accuracy of the model relies heavily on precise wall-pressure spectrum predictions, which are often based on single-equation formulations with adjustable parameters. These parameters are calibrated for particular airfoils and flow conditions and consequently tend to fail when applied outside their calibration range.

This paper introduces a new wall-pressure spectrum empirical model designed to enhance the robustness and accuracy of current state-of-the-art predictions while widening the range of applicability of the model to different airfoils and flow conditions. The model is developed using AI-based symbolic regression via a genetic-algorithm-based approach, and applied to a data set of wall-pressure fluctuations measured on NACA 0008 and NACA 63018 airfoils at multiple angles of attack and inflow velocities, covering turbulent boundary layers with both adverse and favorable pressure gradients. Validation against experimental data (outside the training data set) demonstrates the robustness of the model compared to well-accepted semi-empirical models. Finally, the model is integrated with Amiet's theory to predict the aeroacoustic noise of a full-scale wind turbine, showing good agreement with experimental measurements.

1. Introduction

Rotating blades found in wind turbines and propellers generate noise that significantly affects the quality of life of neighboring communities, causing health and physiological problems in humans. Furthermore, noise complicates the communication, reproduction and predator avoidance of marine animals [1–4]. Therefore, noise regulations have arisen in several fields, such as aeronautics, wind energy, and marine propellers [5–8]. This situation has caused significant research efforts to focus on studying and modeling flow-induced noise produced by aerodynamic surfaces.

Flow-induced noise is the most important noise source in several applications such as wind turbines, aircraft, and ships. Trailing-edge noise, also known as airfoil self-noise, is the minimum amount of noise that an aerodynamic surface can produce [9]. This means that it appears in all operational conditions. Due to the importance of trailing-edge noise in several applications, extensive research has been conducted on this topic, covering experiments [10–18] and numerical simulations [19–23], to better understand trailing-edge noise generation mechanisms. Specifically, Howe [24], Doolan and Moreau [25], and Lee et al. [26] present a complete literature review covering theory, experiments, and numerical simulations of trailing-edge noise. Additionally, there is an extensive literature on trailing-edge noise reduction techniques, such as airfoil trailing-edge serrations [27–31] and porous materials [32–36]. From the literature, it is clear the importance of trailing-edge noise, and hence efforts need to be directed to accurately predict airfoil self-noise with fast methods that could be implemented in the design phase of aerodynamic devices.

Trailing-edge noise is caused by the interaction of the turbulent boundary layer with the airfoil's finite trailing edge. Powell [37] deter-

---

* Corresponding author.
E-mail address: l.botero@upm.es (L. Botero-Bolívar).

https://doi.org/10.1016/j.apacoust.2025.110876
Received 13 January 2025; Received in revised form 12 May 2025; Accepted 1 June 2025

mined that trailing-edge noise has three sources: the surface, the edge, and the turbulence convecting in the flow. They determined that the "edge noise" is of the dipole nature, scaling with a power of the Mach number between 4 and 5, and therefore, the most important noise source at very low Mach numbers. A similar explanation was given by Ffowcs Williams and Hall [38]. They determined that while a turbulent boundary layer (without a solid boundary) radiates as a quadrupole noise source that scales with the 8th power of the flow Mach number (M); the interaction of the turbulence with the trailing edge converts the noise source into a dipole that scales with the 6th power of the flow Mach number. As in most applications $M <<1$, reducing the scaling factor with M increases the efficiency of noise radiation with the inflow velocity. In fact, the first modeling of trailing-edge noise consisted on scaling noise intensity with the 5th power of Mach number, which is more efficient than a dipole due to the presence of the leading edge [9,38,37].

The convective turbulence within the boundary layer causes wall-pressure fluctuations. Close to the trailing edge, these fluctuations are scattered in the far field as noise due to the sudden change of impedance at the trailing edge discontinuity [39]. The effect of the trailing-edge discontinuity is to scatter hydrodynamic pressure fluctuations, with large amplitude and small wavelengths ($\lambda = U_c/f$, where U_c is the mean turbulent boundary layer convection speed and f is the frequency), to acoustic waves with small amplitude and large wavelengths ($\lambda = c/f$, where c is the speed of sound). Therefore, to characterize trailing-edge noise, it is fundamental to accurately describe the flow upstream of the trailing edge statistically [40]. This can be appropriately done through the wall-pressure spectrum (WPS). Consequently, semi-analytical trailing-edge noise prediction methods are often based on WPS close to the trailing edge, such as Amiet's theory [41]. Measurements of wall pressure fluctuations close to the trailing edge during experiments are extremely challenging due to the thin trailing edge thickness of wind tunnel models. Numerical simulations are also challenging when trying to resolve turbulent structures near the airfoil walls, resulting in expensive simulations that cannot be used during design optimization procedures. Therefore, finding an accurate and general model for the turbulent boundary layer WPS is fundamental for an accurate and rapid assessment of trailing-edge noise.

The WPS beneath a turbulent boundary layer has a broadband nature and contains information on the flow structures across the boundary layer of both the inner and the outer regions [42]. The low-frequency range is caused by the large structures present in the outer part of the boundary layer and therefore scales with the boundary layer thickness (δ) and the edge velocity (U_e) [42]. The smaller turbulent structures, located close to the wall, are responsible for the wall-pressure fluctuations in the high-frequency range, which scale with the viscous length defined as ν/u_τ, where ν is the kinematic viscosity and u_τ denotes the friction velocity [42,43]. The mid-frequency range is generated by both types of structures coexisting in the boundary layer, and is known as the overlap frequency range. Based on these scalings, several semi-empirical models have been proposed for the turbulent boundary layer WPS [44,43,45–50].

Initially, Corcos [44], Goody [43], and Chase [45] proposed semi-analytical models using empirical constants based on measurements of a flat plate under zero pressure gradient (ZPG). Catlett et al. [46] extended Goody's model by testing three different trailing-edge configurations that change the stream-wise pressure gradient. Rozenberg et al. [47] proposed an empirical model based on Goody's model considering ZPG and adverse pressure gradients (APG); which is reflected in high values of Clauser's equilibrium parameter (β_c) and Cole's wake factor of the velocity profile (Π). The main variation compared to Goodys' model is to replace the boundary layer thickness (δ) by the boundary layer displacement thickness (δ^*) in the normalization of the spectrum and the wall-shear stress (τ_w) by the maximum shearing stress along the normal direction of the boundary layer ($\tau_{\max} = \mu(\mathrm{d}U/\mathrm{d}y)$). Calculating $\tau_{\max}$ then requires the variation of the average velocity across the boundary layer, which is not obtained with fast turnaround methods such as XFOIL. This is the main disadvantage of this model. Kamruzzaman et al. [48] proposed a model combining the Chase-Howe, Goody, and Rozenberg models using a database that included both equilibrium flat plate and non-equilibrium airfoil boundary layers for non-zero pressure gradients. The main contribution is the use of an amplitude scaling function and time scale ratio to predict spectrum decay. Lee [51] developed an empirical WPS for flows with zero and adverse pressure gradients, based on flat plate and airfoil measurements. The main contribution of this model is to better capture the transition from the overlap-frequency range to the high-frequency range, which was demonstrated to highly depend on the pressure gradient. Lee proposed a parameter, function of β_c, to improve the model for this transition. Furthermore, Lee proposed a correction of Rozenberg's model for the spectrum-level amplitude that provides a better agreement in the low- and mid-frequency ranges with the experimental database. The correction aims to improve the prediction for cases of higher pressure gradients. Hu and Herr [49] proposed their model based on measurements of a NACA 0012. They account for the pressure gradient with the boundary layer shape factor instead of Clauser's equilibrium parameter, as in Lee's model. Recently, Pargal et al. [52] proposed a generalized model based on Goody's model, considering direct numerical simulations (DNS), large eddy simulations (LES), and experiments for attached, separated, and reattached boundary layers. The characteristic of this generalized model is the use of the velocity across the boundary layer, which is difficult to model using fast engineering tools. All the models mentioned so far are presented as a single equation with eight parameters that give the shape of the spectrum, besides scaling factors for the level and the frequency. Therefore, the contribution of each semiempirical model has focused on modeling the eight parameters and the scaling factors instead of proposing a completely new model.

Data-driven methods, such as neural networks, have gained interest in modeling WPS in turbulent boundary layers due to the ability of NN to capture complex nonlinear relationships from large data sets without requiring explicit physical assumptions. For example, studies such as Dominique et al. [53] and Arroyo Ramo et al. [54] used artificial neural networks as an alternative approach to improve the robustness of the WPS model and better predict cases with strong pressure gradients compared to the models available in the literature commented on above. Specifically, in these works the neural network was used to predict boundary layer velocity profiles to later model the WPS using the previously defined single equation. The main disadvantage of NN is that they act as a "black box" with limited interpretability and generalizability beyond a specific training data set. In contrast, the symbolic regression approach adopted in this study, utilizing a genetic-algorithm-based method, derives an explicit and physically interpretable empirical model for the wall-pressure spectrum. The symbolic regression approach provides transparent equations that align with physical intuition, unlike the opaque mappings of neural networks. While neural networks excel in data-rich scenarios, their lack of adaptability outside calibrated ranges underscores the advantage of symbolic regression.

Despite the significant effort of the aeroacoustic community, there is no consensus on a WPS model that is general and usable outside its calibration range and can be used with confidence to predict trailing-edge noise in any case [55,56]. The main drawback of the empirical models available in the literature is the strong dependence on the data used to tune the aforementioned eight parameters of the model, limiting their suitability for actual scenarios, such as in rotating wind turbine blades. Additionally, the use of a single equation to predict the entire frequency range of the WPS requires encapsulating a variety of frequency-dependent physics in only one equation. Although this single equation incorporates several terms that are frequency-dependent and exponents that weight some terms along the frequency range, using a single equation limits the accuracy in capturing the different frequency slopes and inflection points. In the approach proposed in this work, we model the different regions of the spectrum with different frequency decays separately, allowing the model to capture the shape of the spectrum more accurately. As mentioned before, each frequency range of a turbulent boundary layer WPS is generated by different flow structures that scale with different quantities of the boundary layer. When using a single equation to model the entire frequency range of the WPS, the physical principle of the generation of wall pressure fluctuations is oversimplified. An alternative approach was followed by Fritsch et al. [57], who used a symbolic regression algorithm to define functions that are coupled in a single equation. Each function has a relative importance within the frequency range in an attempt to better model the different decays present in a WPS. In what follows, we will consider a similar approach.

To overcome the limitations of the available (semi-) empirical models, we propose an empirical model for the wall-pressure spectrum that:

- Predicts independently curves for three frequency bands, which are blended together into one model. This approach enables capturing different physics and renders the model more robust and generalizable (e.g., making the model more robust to predict the curvature around the inflection point in the low-frequency range);
- the model is generated using an AI-based symbolic regression, which is a machine learning method capable of unveiling physically interpretable analytical equations from data, and reduces the need to incorporate prior knowledge about the physical phenomenon (i.e., we do not need to provide any specific equation);
- the considered database consists of experimental measurements that include two different types of airfoil geometries, Reynolds numbers and FPG and APG, which make the model robust to provide a better prediction for cases outside the training data set.

Additionally, we force the model to use as input simple boundary layer parameters, i.e., boundary layer displacement thickness (δ^*), boundary layer momentum thickness (θ), and friction coefficient (c_f), which are parameters that can be obtained with fast turn-around methods such as XFOIL [58], without the need of running costly numerical simulations.

This paper is organized as follows. Section 2 addresses the methodology followed to propose the WPS model, including the definition of the model, the machine learning approach, and wind tunnel experiments. Section 3 presents the WPS model. Section 4 shows the validation of the model with other airfoil data available in the literature and a complete wind turbine. Finally, Section 5 presents the main conclusions of this research.

2. Methodology

2.1. Wall-pressure spectrum definition

The WPS (Φ_{pp}) is divided into three frequency bands: low-frequency, mid-frequency, and high-frequency, that is, $\Phi_{\mathrm{pp|LF}}$, $\Phi_{\mathrm{pp|MF}}$, and $\Phi_{\mathrm{pp|HF}}$, respectively, which are delimited by f_2 and f_3, as shown in Fig. 1. f_2 limits the low- and mid-frequency bands, and is defined as the frequency of the maximum spectral level along the entire frequency range. f_3 limits the mid- and high-frequency ranges. f_3 is defined as the frequency at which the decay of the WPS level as a function of frequency changes significantly, suggesting that a different physical phenomenon dominates the WPS.

To obtain f_3, the experimental spectrum was divided into frequency bins of 500 Hz; the center of the bin was progressively moved by 240 Hz. The spectrum slope for each bin was calculated by fitting a first-order polynomial to the logarithmic values of the spectral level and the frequency. f_3 is considered where the slope deviates by more than 5% from the value of the previous bin. f_1 and f_4 define the frequency range in which the WPS is calculated. Those frequencies do not affect the model itself but are needed to blend the curves of each frequency band into a single curve. f_1 is defined as $0.5 f_2$ and f_4 is defined as the highest frequency limit where the WPS is calculated. For the training data set, it is defined as 5 kHz to avoid contamination of electronic noise during the experimental measurements.

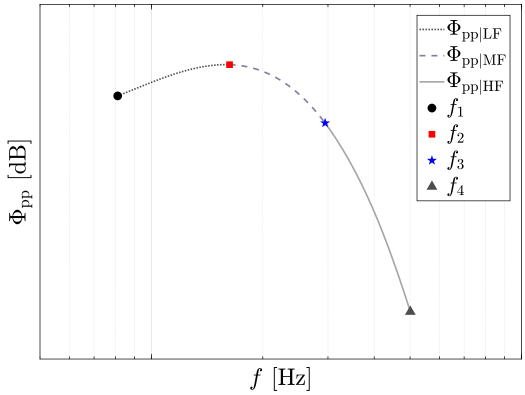

Fig. 1. Frequency bands of a generic WPS.

Each frequency band was modeled independently on the logarithmic scale using the symbolic regression approach, where we obtained three equations. The inputs given to the symbolic regression algorithm to model the spectrum are the inflow velocity (U), boundary layer thickness (δ), boundary layer displacement thickness (δ^*), boundary layer momentum thickness (θ), wall shear stress (τ_w), and the pressure gradient ($\mathrm{d}C_p/\mathrm{d}x$). This set of parameters was chosen for two main reasons. The first one is that all these variables can be easily obtained for a specific airfoil without running expensive simulations (e.g., using fast panel method solvers such as XFOIL). Secondly, these parameters are chosen to be as general and independent as possible. Although other models include additional variables (such as $\Delta = \delta/\delta^*$, or $\beta = (\delta^*/\tau_w)(\mathrm{d}p/\mathrm{d}x)$), they are not retained in this work since they can be defined as a combination of the previously selected ones and therefore could introduce a bias in the model, providing a solution which is not optimal.

The limiting frequencies (f_2 and f_3) are modeled using the same inputs, and the equations obtained for each frequency band are combined through a weighted average as a function of the frequency, as will be explained in the following sections.

2.2. Symbolic regression approach

Symbolic regression (SR) has emerged in recent years as an alternative to traditional regression algorithms to derive models from data (fitting data). While the traditional approach is based on a user-defined function, with some tunable coefficients that can be adjusted to minimize the error between the function and the data, the SR approach allows us to discover new functions from scratch. The main idea is to provide mathematical operators to the algorithm that can be combined automatically to define the best equation to fit the data. This way of solving problems involves a change in the current paradigm and provides an alternative to rediscover formulations of physical laws [59], among other applications. A main advantage of SR is that it does not require a priori specification of the model, and hence it is not affected by human bias or unknown gaps in domain knowledge. Although this family of algorithms was developed in the early 1990s, recent advancements in machine learning and the rapid improvement of computing power have fostered the use of SR for different fields; such as wind turbine wake modeling [60], astrophysics [59], turbulence [61], discovery of missing terms in differential equations [62], material science [63] and prediction of solar power production [64], among others. The application of SR in the field of acoustics has gained importance in recent years, as some advances have been made in the prediction of sound propagation in shallow water environments [65] and in the modeling of noise generation for porous airfoils [66]. Also, recent advancements in rotor noise prediction [67,68] use Gene Expression Programming to generate analytical noise spectrum models. Although some attempts have been made in the

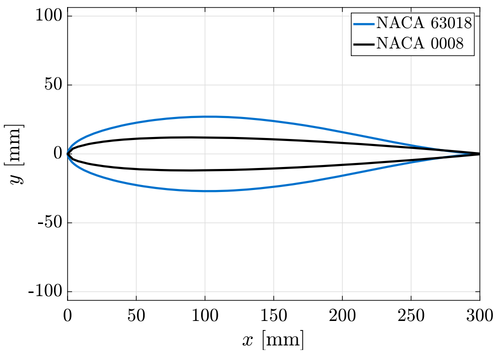

Fig. 2. Airfoils' coordinates.

reconstruction of the WPS model through symbolic regression [69,57] and neural networks (NN) [53,70], these models are difficult to generalize (for SR-based approaches) and lack interpretability (in the case of using NN).

In this work, SR is used to discover mathematical expressions to model the turbulent boundary layer WPS of two airfoils. The algorithm training is performed on the basis of experimental data (detailed in the following sections). Furthermore, the set of allowed variables are inflow conditions and boundary layer parameters that can be easily defined/obtained, allowing for a generalizable approach.

Symbolic regression algorithms are based on the main idea of continuously constructing new analytical functions, constrained by the user's input, to fit a set of data. These functions are created by using a set of operators (e.g., $+$, $-$, $*$, $/$, ...), functions (e.g., abs(), sin(), log(), ...) and variables (e.g., x, t, ...) that the user must decide beforehand. The resulting solution is formed by a combination of these operators and variables in a specific order. Another key aspect of SR is the *complexity* of the solution. If no constraints were applied to limit the complexity, very long equations with poor interpretability could be created. Therefore, the complexity of the final solution is usually constrained by defining the maximum length of the new functions. Furthermore, low-complexity functions are less prone to overfitting, leading to more generalizable solutions.

During training, new functions are created continuously, guided by an optimization algorithm, with the final objective of minimizing the loss between the discovered solution and the real data. The generation process consists of solving an optimization problem, which is usually handled by genetic algorithms, where the function itself is mutated by modifying its components and the interrelation among them. In the present work, we apply the methodology implemented by Cranmer [71], who provides an open-source code with a multi-population evolutionary algorithm to solve the SR problem in an efficient and modular way. This approach has been thoroughly tested and is capable of exceeding several state-of-the-art open-source symbolic regression algorithms. This original implementation is based on genetic algorithms for optimization [72] at its core, but includes additional features to improve performance, such as simulated annealing [73], classic Broyden–Fletcher–Goldfarb–Shanno (BFGS) optimization algorithms [74], and a novel adaptive parsimony metric. These improvements are combined with an asynchronous programming approach and multithreading parallelization, enhancing the overall performance and reducing the simulation time.

2.3. Experimental database

The symbolic regression algorithm is applied to wall-pressure fluctuation measurements of a NACA 0008 and a NACA 63018 of 300 mm chord (c). The geometry of the airfoils is shown in Fig. 2. The WPS is measured at 95% of the chord of each airfoil on both the suction and pressure sides. The test conditions for each airfoil are shown in Table 1, where α_g is the geometric angle of attack (the effective angle of attack α_e is calculated as explained in Section 2.4.2), U is the inflow velocity, and Re is the Reynolds number based on U and c. These conditions provide a total of 76 cases.

Table 1
Experimental test conditions.

Airfoil	α_g [°]	U [m/s]	Re [-]
NACA 0008	0:0.5:6	30	7.3×10^5
	0, 3, 5	10, 30	$\{2.4, 7.3\} \times 10^5$
	0	10:5:45	$\{2.4{:}1.2{:}10.1\} \times 10^5$
NACA 63018	0:1:7	10, 30	$\{2.4, 7.3\}\times 10^5$
	0	10:5:45	$\{2.4{:}1.2{:}10.1\} \times 10^5$

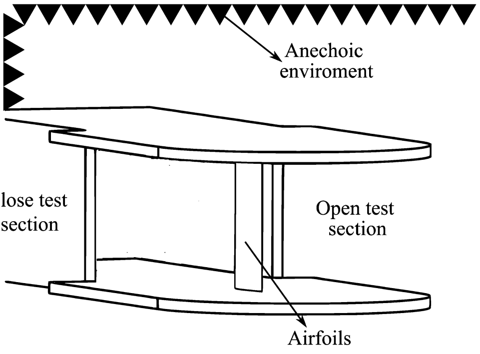

Fig. 3. Schematic view of the experimental set-up.

For the high-frequency band, only the cases where f_3 <4 kHz were considered (see Fig. 1 for the definition of f_3). This is to guarantee that there are enough data in the high-frequency band to model this part of the spectrum due to the limitation of the measurements up to 5 kHz mentioned before. This constraint does not affect the proposed WPS model, but reduces the number of cases that are considered to model the high-frequency band to 47.

2.4. Wind tunnel experiments

2.4.1. Wind tunnel

The experiments were carried out in the aeroacoustics wind tunnel of the University of Twente. The facility is a closed circuit wind tunnel, which has a 0.9 m width and 0.7 m height close and open test sections. The wind tunnel has a contraction ratio of 10:1 and seven screens that keep the turbulence intensity below 0.08% with velocities up to 60 m/s [75]. The test section is enclosed by an anechoic chamber of 6 m × 6 m × 4 m. The empty anechoic chamber has a cut-off frequency of 160 Hz. The temperature in the test section is controlled at approximately 20 °C. The airfoils were vertically installed in the open test section using two rotatory end plates, allowing changes in the angle of attack of 0.5° precision. More information on the wind tunnel can be found in de Santana et al. [75]. Fig. 3 shows a schematic representation of the experimental setup.

2.4.2. Wind tunnel corrections

The wind tunnel experiments were conducted in an open jet test section. Therefore, the geometric angle of attack (α_g) was corrected to obtain the effective angle of attack (α_e). The corrections were based on the approach proposed by Brooks et al. [76].

$$\sigma = (\pi^2/48)(c/W)^2; \qquad d\sigma = (1+2\sigma)^2 + \sqrt{12\sigma}; \qquad \alpha_e = \alpha/d\sigma; \tag{1}$$

where W is the wind tunnel width. All data and analyses are presented in relation to the effective angle of attack.

2.4.3. Boundary layer transition

The boundary layer transition was forced at 6.5% of the chord, using zigzag strips of 60° zigzag angle and 12 mm width. The trip height (k) was varied with the inflow velocity and the angle of attack to keep the ratio k/δ_k between 0.4 and 0.6 for all cases, where δ_k is the boundary layer thickness at the trip location. δ_k was estimated using XFOIL simulations [58], using the approach explained in Section 2.5. For this particular situation (to calculate δ_k and estimate the trip height), XFOIL simulations were conducted using natural transition with the critical number, calculated based on the wind tunnel inflow turbulence (Tu = 0.08% [75]):

$$N_{\mathrm{crit}} = -8.43 - 2.4\log(Tu/100). \tag{2}$$

Note that XFOIL simulations for obtaining the boundary layer parameters at the airfoils' trailing edge needed for proposing the WPS model are conducted with forced transition, similar to the experiments, as it is specified in Section 2.5.

2.4.4. Measurement of wall-pressure fluctuations

The airfoils are instrumented with 82 remote microphone probes (RMP) distributed along the chord and the span. The wall-pressure fluctuations are measured on both the suction and pressure sides at 95% of the chord. These measurements were used to propose the model. Additionally, twelve RMP are distributed along the span at 97% of the chord which were used to verify the statistical similarity of the flow in the spanwise direction. The WPS of the twelve microphones matched within 1 dB.

Remote microphone probes consist of pinholes of 0.3 mm diameter on the airfoil surface connected to a unique stainless steel tube of 1.6 mm inner diameter. A tube assembly outside the model connects the tubes to the microphones and the anechoic termination, i.e., a plastic tube of 1.6 mm inner diameter and 3 m long. The extreme of the anechoic termination was sealed to avoid airflow passing through the tube because of the difference in pressure between the airfoil surface and the environment. On the side of the tube assembly, Knowles FG 23329-P07 microphones are connected. The junctions of the stainless steel tube, the anechoic termination, and the microphones with the tube assembly were sealed to prevent leakage, which was verified during the calibration of each RMP. The calibration of RMPs is explained in Appendix A. More information on the technique can be found in dos Santos et al. [77].

Four National Instruments PXIe-4499 Sound and Vibration modules installed on a NI PXIe-1073 chassis were used to sample the surface microphones. The microphone data was acquired during 30 s with a sampling frequency of 65536 (2^{16}) Hz. The WPS was calculated by adopting the Welch method, using a window size of 2^{14} samples (7.5 s) and a Hanning windowing method with 50% overlap, which resulted in a bin size of 8 Hz. The WPS is presented in dB, calculated according to Glegg and Devenport [42]. The reference pressure and delta frequency for normalizing the power spectral density were 20 μPa and 1 Hz.

2.5. XFOIL simulations

XFOIL simulations were performed replicating the conditions of the wall-pressure fluctuations measurements to obtain the parameters of the boundary layer close to the trailing edge needed to propose the model. The input parameters for XFOIL were the airfoil geometry, the Reynolds number, calculated on the basis of the airfoil chord and inflow velocity, the Mach number, the effective angle of attack, and the location of the forced transition (i.e., 0.065). The boundary layer parameters were extracted from XFOIL simulations at x/c =0.95, i.e., the same location of the wall-pressure fluctuations measurements.

XFOIL calculates the displacement thickness (δ^*), momentum thickness (θ), and skin friction coefficient (C_f). The boundary layer thickness (δ) is calculated as [58]:

$$\delta = \theta\left(3.15 + \frac{1.72}{H_k - 1}\right) + \delta^*, \tag{3}$$

where H_k is the kinematic shape parameter:

$$H_k = \frac{H - 0.290M_e^2}{1 + 0.113M_e^2}, \tag{4}$$

with M_e the boundary layer edge Mach number, and H the shape parameter given as $H = \delta^*/\theta$. For low Mach number flows, H_k given by Eq. (4) reduces to H. This approximation is used in this study.

The friction velocity, u_τ, is calculated as:

$$u_\tau = \sqrt{\tau_w/\rho}, \tag{5}$$

where $\tau_w = 0.5\rho U^2 C_f$. Finally, the pressure gradient $\mathrm{d}C_p/\mathrm{d}x$ is calculated using the central differencing scheme, with the x/c =0.95 as the central value.

XFOIL simulations are validated against experiments by comparing δ, δ^*, θ, and u_τ close to the trailing edge, and C_p distribution along the chord. This validation is shown in Appendix B. There is a good agreement between XFOIL and the experiments.

Table 2
Hyperparameters of the symbolic regression algorithm during the training.

General parameters	
Population size	200
Iterations	50
Crossover probability	0.0259
Perturbation factor	0.129
Annealing constant	3.17
Mutation parameters	
Mutate constants	0.0346
Mutate operators	0.293
Swap operands	0.198
Rotate tree	4.26
Add node	2.47
Insert node	0.0112
Delete node	0.87
Simplify	0.00209
Randomize	0.000502
Do nothing	0.273
Optimize	0.0
Form connection	0.5
Break connection	0.1

3. Wall-pressure spectrum model

The SR-based WPS model is defined based on a set of operators, functions, and variables that the SR algorithm is allowed to use when generating new functions. In this case, we will try to minimize the number of available degrees of freedom, as the objective is to obtain a simple and interpretable final solution:

1. **Operators:** $+$, $-$, $*$ and $/$.
2. **Functions:** $\mathrm{pow2}(x) = x^2$, $\mathrm{abs}(x) = |x|$.
3. **Variables:** f, U_e, δ, δ^*, θ, τ_w and $\mathrm{d}C_p/\mathrm{d}x$.

Furthermore, the maximum complexity of an equation is set to 25, where the use of each operator, function, or variable increases the complexity by 1 unit. Also, the algorithm is allowed to include real constants, but each constant will increase the complexity by 2 units.

The initial population of functions is formed by 200 individuals and the multi-population genetic algorithm runs 50 iterations for each function to be discovered. A summary of the most relevant hyperparameters is presented in Table 2. It is important to notice that, before the training, all mutation parameters are normalized; that is, the sum of all of them must be 1 unit. The loss during training is computed as the L_2 norm $||x - x^*||_2$ between the original data x and the generated function x^*, within the current frequency band.

The WPS in each frequency band is modeled in logarithmic scale and consequently expressions must begin with a $10\log_{10}(\bullet)$. Moreover, on the basis of the experimental data, the high-frequency region has an almost linear decay on a logarithmic scale; hence, we force a linear decay in the high-frequency band. As a result of the SR process, the following set of equations are discovered to model/calculate the WPS in each frequency band (see Fig. 1), and the limit frequencies:

$$
\begin{aligned}
f_1 &= 0.5 f_2;\\
f_2 &= 0.22/\delta^* + 0.045\ U_e/\delta^*;\\
f_3 &= 997 + 0.26\ U_e/\delta;\\
f_4 &= 5000;\\
\Phi_{\mathrm{pp|LF}} &= 10\log_{10}\left(0.16\left(\delta U_e\right)^2\right);\\
\Phi_{\mathrm{pp|MF}}(f) &= 10\log_{10}\left(\left(\frac{f}{f_2}\right)^{\frac{b}{3}}\right) + \left(\frac{\Phi_{\mathrm{pp|LF}} + offset_{\mathrm{MF}}}{2}\right);\\
b &= -\left|\tau_w - 1804.5\theta\right|;\\
offset_{\mathrm{MF}} &= 10\log_{10}\left(4.41\cdot 10^{-4}\frac{U_e\left(\tau_w - U_e\right)^2}{f_2}\right);\\
\Phi_{\mathrm{pp|HF}}(f) &= 10\log_{10}\left(\left(\frac{f}{f_3}\right)^{b}\right) + \Phi_{\mathrm{pp|MF}}(f_3).
\end{aligned}
\tag{6}
$$

To obtain a single equation that models the WPS in the entire frequency range, the WPS for each band are linearly weighted with the frequency, as:

$$
\begin{aligned}
\Phi_{\mathrm{pp|LMF}} =& \Phi_{\mathrm{pp|LF}}\frac{\log_{10}(f_3) - \log_{10}(f)}{\log_{10}(f_3) - \log_{10}(f_1)}\\
&+ \Phi_{\mathrm{pp|MF}}\frac{\log_{10}(f) - \log_{10}(f_1)}{\log_{10}(f_3) - \log_{10}(f_1)};\\
\Phi_{\mathrm{pp|MHF}} =& \Phi_{\mathrm{pp|MF}}\frac{\log_{10}(f_4) - \log_{10}(f)}{\log_{10}(f_4) - \log_{10}(f_2)}\\
&+ \Phi_{\mathrm{pp|HF}}\frac{\log_{10}(f) - \log_{10}(f_2)}{\log_{10}(f_4) - \log_{10}(f_2)};\\
\Phi_{\mathrm{pp}} =& \Phi_{\mathrm{pp|LMF}}\frac{\log_{10}(f_4) - \log_{10}(f)}{\log_{10}(f_4) - \log_{10}(f_1)}\\
&+ \Phi_{\mathrm{pp|MHF}}\frac{\log_{10}(f) - \log_{10}(f_1)}{\log_{10}(f_4) - \log_{10}(f_1)}.
\end{aligned}
\tag{7}
$$

Initially, the low- and mid-frequency bands are combined between f_1 and f_3, obtaining $\Phi_{\mathrm{pp|LMF}}$; and the mid- and high-frequency bands are combined between f_2 and f_4, obtaining $\Phi_{\mathrm{pp|MHF}}$. Later, $\Phi_{\mathrm{pp|LMF}}$ and $\Phi_{\mathrm{pp|MHF}}$ are combined between f_1 and f_4 using the same approach.

The frequency f_2 depends on the inflow velocity and boundary layer displacement thickness, whereas f_3 depends on the boundary layer thickness instead. The equation for the low-frequency range ($\Phi_{\mathrm{pp|LF}}$) is a constant (non-dependent on the frequency, f) that gives the level of the WPS, as a function of the boundary layer thickness and the inflow velocity. The high-frequency band ($\Phi_{\mathrm{pp|HF}}$) is a logarithmic straight line with a decay b that depends on the wall shear stress and momentum thickness. The decay for the mid-frequency band ($\Phi_{\mathrm{pp|MF}}$) is one-third of that of the high-frequency band. Both equations have an offset to set the level of the curve. The offset in the mid-frequency range ($offset_{\mathrm{MF}}$) depends on velocity, wall shear stress, boundary layer thickness, and f_2. To reduce the discontinuity of the curve at f_2, where the LF and MF regions blend together, the mid-frequency offset is averaged with the value of the low-frequency band. The offset in the high-frequency band is simply the value of the WPS given by the expression of the mid-frequency range evaluated at $f = f_3$ ($\Phi_{\mathrm{pp|MF}}(f_3)$).

The model obtained is shown in Fig. 4, where the influence of the boundary layer parameters on the WPS is detailed. The boundary layer thickness (δ) and displacement thickness (δ^*) affect the level and position of the maximum spectral level, while there is no effect in the high-frequency band. As the boundary layer thickens, the energy content of the WPS increases and shifts towards lower frequencies. In contrast, momentum thickness (θ) and wall-shear stress (τ_w) affect the level and decay of the high-frequency range. The energy content of the WPS increases and shifts towards higher frequencies as τ_w increases, whereas it decreases as θ increases. This behavior agrees with theory since wall pressure fluctuations in the low-frequency range are caused by larger turbulent structures that scale with δ, while fluctuations in the high-frequency range relate to small turbulent structures that scale with the viscous length (ν/u_τ), which has a direct relationship with τ_w. In addition, the edge velocity (U_e) increases the WPS level throughout the frequency range, as expected. Furthermore, the inflow velocity slightly shifts the energy content towards higher frequencies (see the shift in the maximum in Fig. 4e), which is also in agreement with the theory [42].

Similar tendencies of the WPS model with boundary layer parameters are found in the literature, e.g., Lee [51], except for the specific case of θ. In the reference, θ shows a trend similar to δ and δ^*, whereas in our model θ has an effect only in the high frequency range and opposite to δ. According to Fig. 5b, the experimental results show a similar trend to the reference, i.e., increasing θ increases the spectral level. The different trend of θ in our model compared to the reference is due to the negative sign in the definition of b, that reduces the value or the effect of τ_w to calculate the decay of the wall-pressure spectrum. Note that in the sensitivity analyses we vary a single parameter while keeping the others constant, which is not realistic since all the boundary layer parameters change simultaneously. Therefore, the different trend does not mean a wrong capturing of the physics

Fig. 5 shows some measured WPS within the training dataset for several conditions of inflow velocity and angle of attack of both airfoils to show the dependency of the WPS on boundary layer parameters. Figs. 5a and 5b show the WPS for several angles of attack at 10 m/s inflow velocity. As the angle of attack increases, the pressure gradient increases, causing an increase in the boundary layer thickness and displacement thickness [58]; this makes the frequency content of the WPS shifts to lower frequencies due to the increase in size of the turbulent structures within the boundary layer. Therefore, for thicker boundary layers, there is a higher spectral level in the low-frequency range, as observed for both airfoils and predicted by the model (Fig. 4a). At the same time, an increase in the angle of attack reduces the wall-shear stress [58], and consequently the level in the high frequency range is reduced. Furthermore, in the high-frequency range, the opposite behavior of the wall-shear stress and boundary layer displacement thickness, which is represented in the model by the subtraction symbol in the definition of b and in the different trend observed in Figs. 4c and 4d.

The inflow velocity (or edge velocity) has an influence in the entire frequency range, as predicted by our model in Fig. 4e and shown by the experiments in Fig. 5c for the NACA 0008 airfoil. In both figures, it is noticeable that besides increasing the spectral level in the entire frequency range, the energy content, i.e., the maximum spectral level along the frequency, is shifted towards higher frequencies. This is due to the reduction of the boundary layer thickness as a function of the inflow velocity; which is also reflected in our model in the definition of f_2 and f_3, where the boundary layer thickness and displacement thickness are in the denominator. To see the effect of the inflow velocity clearer, the WPS for the NACA 63018 at several velocities are scaled. The spectral level is scaled using a power of two of the velocity, and the frequency is scaled using the factor δ/U_e, see Fig. 5d. According to the figure, the spectral level roughly scales with a power of two with the inflow velocity, which is represented in our model by the term $(\delta U_e)^2$ in the definition of $\Phi_{\mathrm{pp|LF}}$ that gives the level of the WPS. Furthermore, the frequency of the spectrum scales with δ/U_e, showing that the dependence of f_2 and f_3 with these parameters is also correct. It is important to mention that, aside from the sensitivity analysis conducted in Fig. 4,

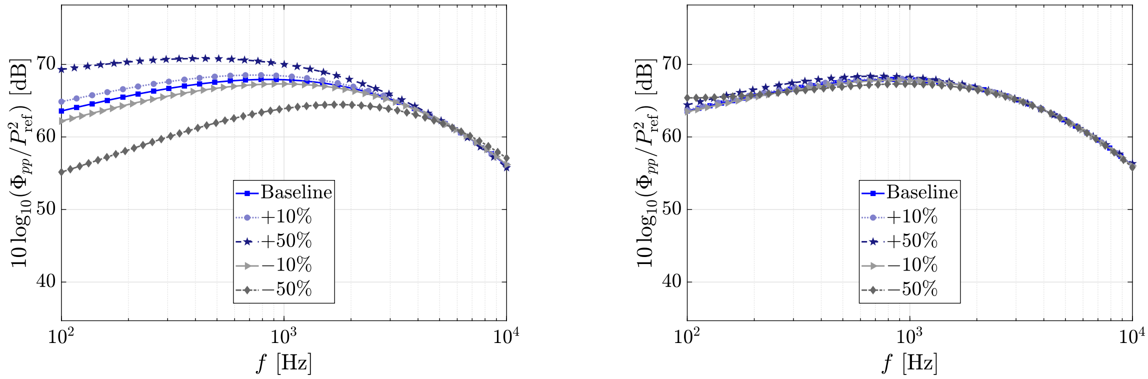

(a) Boundary layer thickness, δ

(b) Boundary layer displacement thickness, δ^*

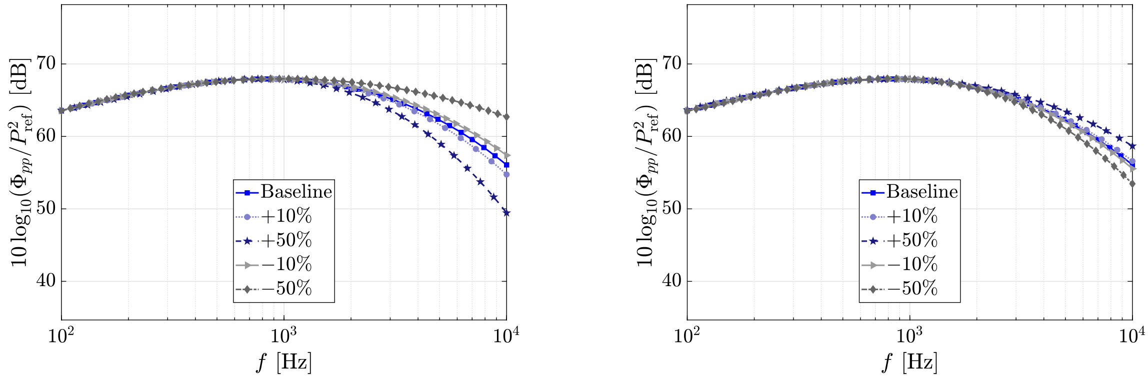

(c) Boundary layer momentum thickness, θ

(d) Wall shear stress, τ_w

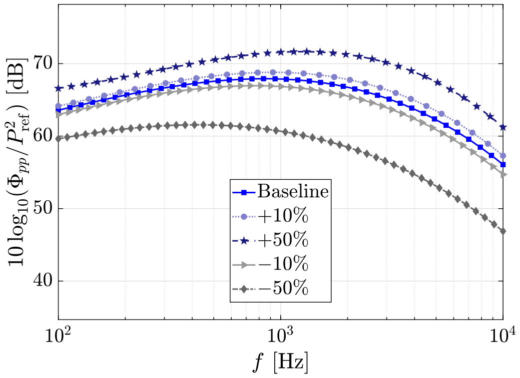

(e) Edge velocity, U_e

Fig. 4. Sensitivity of the boundary layer parameters on the predicted wall-pressure spectra. $P_{\mathrm{ref}} = 20$ µPa.

where a single parameter was modified while the others were kept constant, in the experiments a variation of the angle of attack and inflow velocity changes the boundary layer development, and therefore, all the parameters of the boundary layer close to the trailing edge are modified. Therefore, it is not absolutely precise to define the influence of a single parameter when the others are being also modified.

Fig. 6 shows the WPS estimated with our model and with Lee's and Kamruzzaman's models scaled with the outer boundary layer scales (δ/U_e) and the inner scales (ν/u_τ^2) of the boundary layer. The models are compared with the well-established power-law regions of the WPS, i.e., $(\omega\delta/U_e)^{-2}$ for the low-frequency range and $(\omega\nu/u_\tau^2)^{-5}$ for the high-frequency range [42,45,78]. When scaling with the outer scales (Fig. 6a), the three models present a rolloff between 2 and 2.5, which is quite close to the expected decay (2). In particular, our model shows a decay of 2.5. When scaling with the inner scales, our model presents a decay with a power of -5, likewise expected. The same decay is observed for the Lee model. In contrast, Kamruzzaman's model presents a decay closer to 4. The fact that there is a similar decay of the level as a function of the frequency among the models and in agreement with the experiments shows that our model preserves the physics that generates the wall-pressure spectrum. It is worth noticing that there is a big difference in the scaled level of the WPS; this is due to the level constants that are established empirically in every model.

3.1. Error assessment between the experiments and the symbolic regression model

The error is measured as the squared difference between the predicted ($\Phi_{\mathrm{pp|mod}}$) and measured ($\Phi_{\mathrm{pp|meas}}$) WPS (in dB), weighted by the frequency to account for the logarithmic scale. If the error is not weighted to account for the logarithmic scale on the frequency axis, the low-frequency band, where there are few data points, would have a

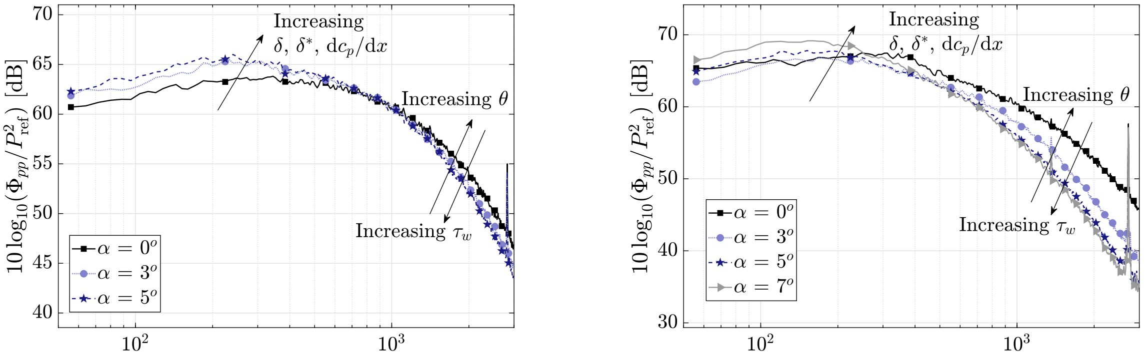

(a) Naca 0008. U =10 m/s

(b) Naca 63018. U =10 m/s

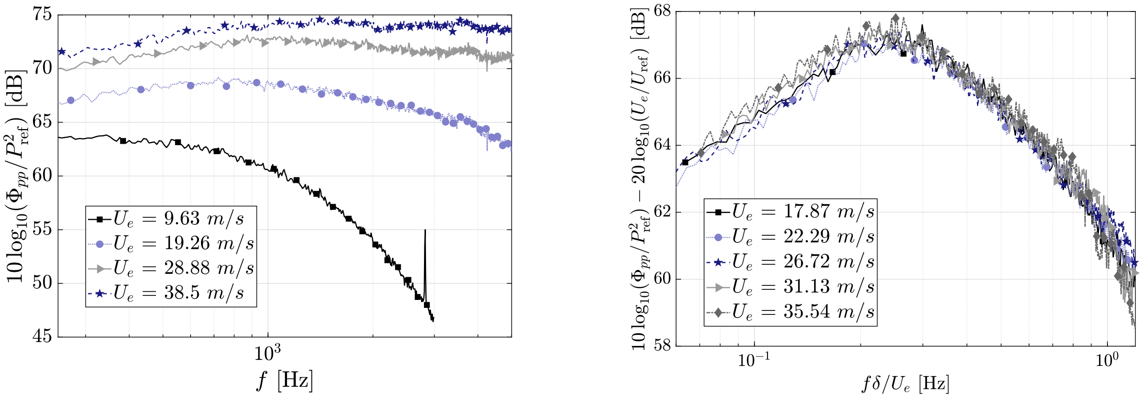

(c) Naca 0008. α =0°

(d) Naca 63018. α =0° (scaled)

Fig. 5. Measured WPS for several conditions of inflow velocity (U) and angle of attack (α). U_{ref} =10 m/s.

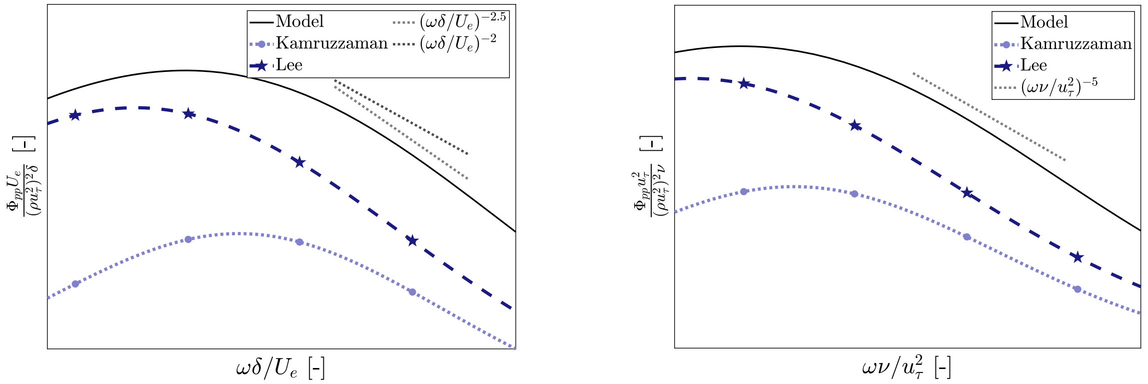

(a) Scaling with outer scales

(b) Scaling with inner scales

Fig. 6. Wall-pressure spectrum model scaling with inner and outer scales.

low impact in the error, while the high-frequency band, where there are many points, would have a higher impact. As the model should be able to fit the experiments in all frequency bands, a correction must be applied. Therefore, starting from the definition of the integral formulation of mean squared error, we derive a modified version of the error that takes this fact into consideration. The standard integral formulation of the mse is defined as:

$$mse = \frac{1}{f_{\max} - f_0} \int_{f_0}^{f_{\max}} \left(\Phi_{\mathrm{pp|meas}} - \Phi_{\mathrm{pp|mod}}\right)^2 \, \mathrm{d}f; \tag{8}$$

Now, we change the integration variable from f to $log(f)$ to balance all frequency bands:

$$mse_{log} = \frac{1}{\log(f_{\max}) - \log(f_0)} \int_{\log(f_0)}^{\log(f_{\max})} \left(\Phi_{\mathrm{pp|meas}} - \Phi_{\mathrm{pp|mod}}\right)^2 \, \mathrm{d}\log(f); \tag{9}$$

Finally, we rewrite the integral to have the frequency in the integration limits and as the differential variable:

$$\mathrm{Error} = \frac{1}{\log\left(\frac{f_{\max}}{f_0}\right)} \int_{f_0}^{f_{\max}} \frac{1}{f} \left(\Phi_{\mathrm{pp|meas}} - \Phi_{\mathrm{pp|mod}}\right)^2 \, \mathrm{d}f; \tag{10}$$

where log is the natural logarithm, and f_0 and $f_{\max}$ are the minimum and maximum frequencies where the overall spectrum is calculated. To

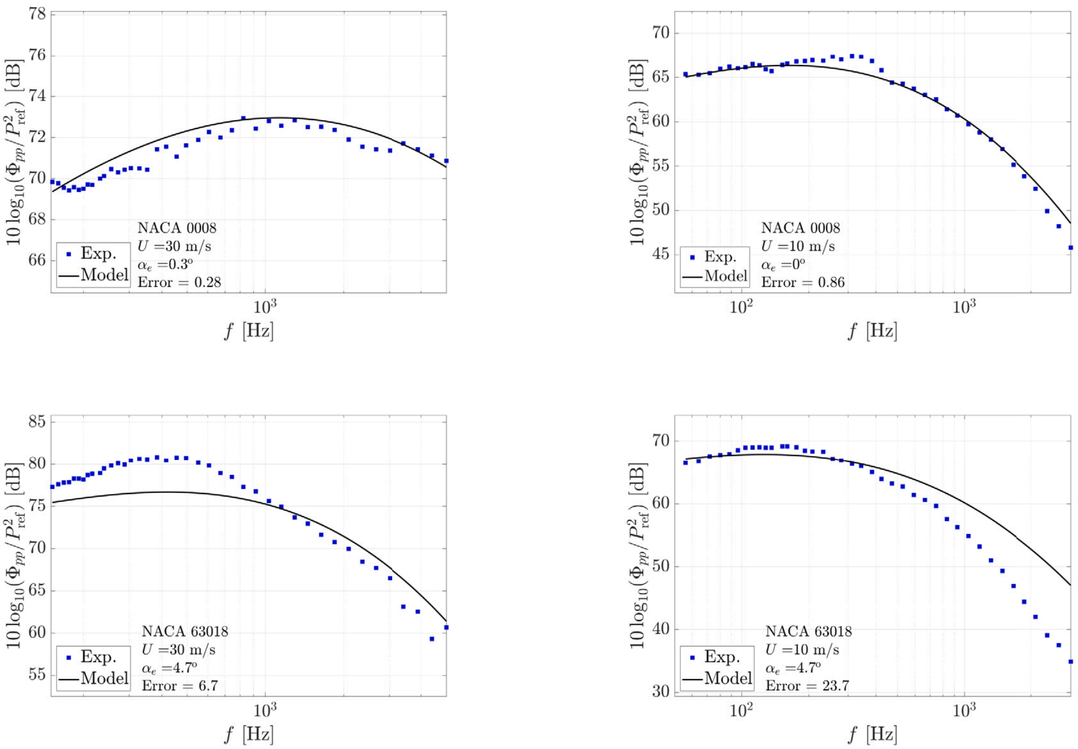

Fig. 7. Predicted and measured WPS of several cases from the training data set.

Table 3
Error of the model for the training data set.

Cases / Error	APG & LF	FPG & LF	APG & HF	FPG & HF
Error$_{\mathrm{min}}$	0.16	0.23	0.70	0.49
Error$_{\mathrm{max}}$	22.9	11.09	7.28	11.01
Error$_{\mathrm{mean}}$	3.087	2.48	2.66	2.87

apply this error to a discrete data base, the integral should be discretized using a numerical method (e.g., trapezoidal rule, Simpson's rule, etc.).

Table 3 shows the error statistics of the model for the training data set calculated with Eq. (10). Note that the error is segregated into favorable (FPG) and adverse (APG) pressure gradients; and between low-frequency (LF) and high-frequency (HF) bands, since the size of the data set was different, ref. to Section 2.3. The error is similar for the four groups of cases, showing slightly better results for the APG (lower mean and maximum values). For completeness, in Fig. 7 the measured and predicted WPS for four cases within the data set are shown, with the associated errors that range from the minimum to maximum (see Table 3). The precision of the model slightly decreases with the angle of attack; however, it agrees with the experimental results in the entire frequency range with a margin of 4 dB.

4. Validation of the model outside the training data set

The model is validated by comparing the predictions with published experimental data and classic semi-empirical models. Later, acoustic predictions for a full-scale wind turbine are also presented and compared to field measurements.

We challenge the model with predictions outside the range of the training data set and explore how it generalizes for Reynolds numbers, angle of attack, airfoil geometry, and frequency ranges outside the range of the training set. Now, the Reynolds number range is $\{0.26 - 1.5\}\cdot 10^6$ compared to $\{0.26 - 0.90\}\cdot 10^6$ of the training data set. The maximum angle of attack is 10.3° compared to 7° in the data set. More importantly, three different airfoil geometries are used for validation: NACA 0012, NACA 0018, and DU-96-W-180. Furthermore, experiments were conducted in a different experimental setup.

Fig. 8 shows the measured WPS (Exp. in the legend) compared with our model (model in the legend), together with the Kamruzzaman model [48], Lee model [79], Goody model [43], and the symbolic regression-based model proposed by Fritsch et al. [57]. The specific conditions for each validation case are summarized in Table 4, together with the error (calculated following Eq. (10)), and the reference of the experimental data.

In general, the proposed model shows good agreement for all cases. The best agreement is obtained for cases B, C, and G, with errors lower than the average error of the training data set. The worst case is for case E ($\alpha = 10.3^\circ$), where there is a significant discrepancy between the model and measurements for $f > 1$ kHz. However, our model predicts well the low-frequency hump expected for high angles of attack [80,81]. The main reason for the poor agreement in the high-frequency range is that τ_w, which significantly affects the spectrum rolloff in the high frequency (see Fig. 4d), is obtained with XFOIL simulations instead of experimental measurements as the other parameters (δ, θ, δ^*) that are reported in Suryadi and Herr [80]. Reference [80] also shows that the precision of XFOIL simulations at high angles of attack is reduced. Even though case E is the worst case for our model, it presents the lowest error among all models, which shows that the model is robust enough and can be extrapolated even for complex scenarios.

Compared with the other semi-empirical models, our model also performs well. There are some specific cases where other approaches present a better agreement with the measurements than our model, such as, Lee model for cases A and F, and Kamruzzaman model for case D. However, our model presents the lowest average error among all the models. Furthermore, our model is the most robust since the error variability is the lowest among the models and the maximum error is also the lowest. In particular, the model proposed by Fritsch et al. [57] does not show good behavior for the particular cases presented here, mainly because of the divergence at high frequencies. This frequency divergence was avoided in our model because of the constraints imposed in the training process of the symbolic regression algorithm, where we enforce

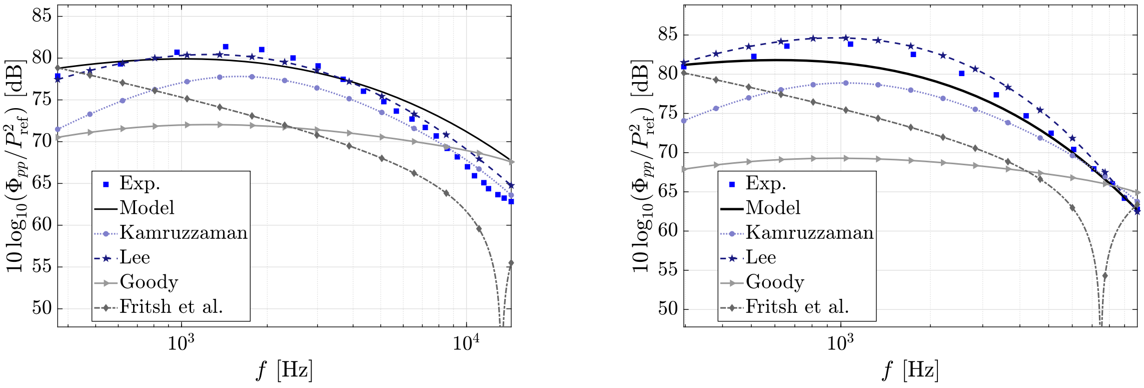

(a) Case A

(b) Case B

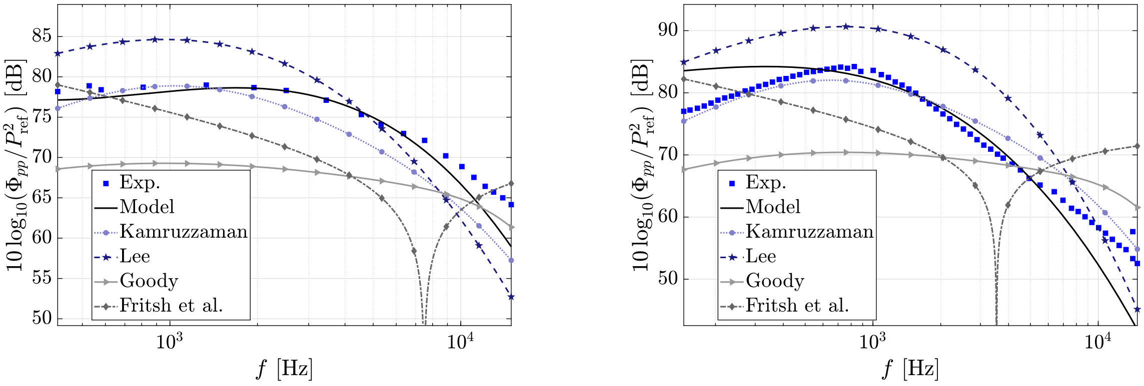

(c) Case C

(d) Case D

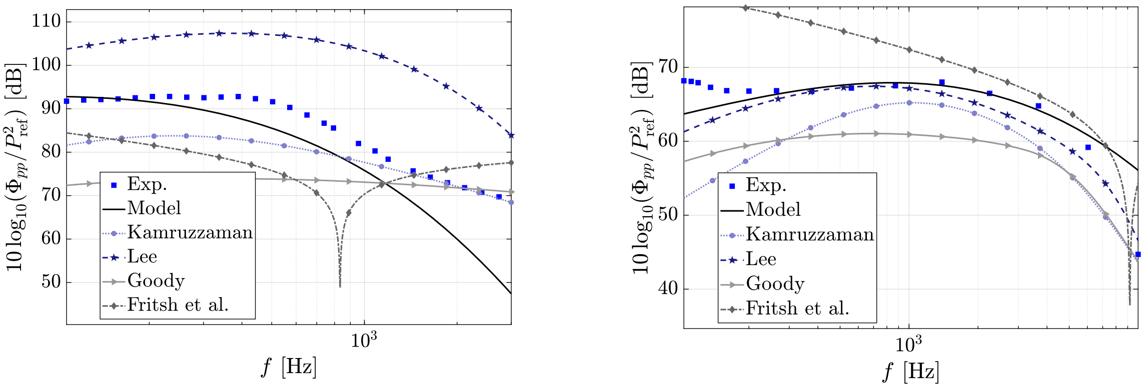

(e) Case E

(f) Case F

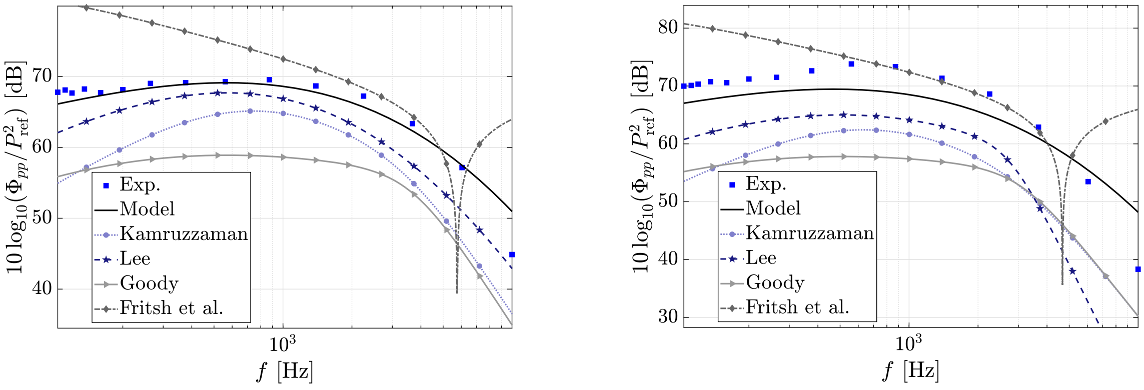

(g) Case G

(h) Case H

Fig. 8. Comparison of the predicted and measured WPS for several conditions outside the training data set.

Table 4
Error of several models compared to experimental measurements outside the training data set.

Name	Conditions	Error				Ref.
		Kamruzzaman	Lee	Goody	Model	
Case A	NACA 0012; $U_\infty = 56$; $c = 0.4$; $\alpha = 0^o$	11.54	**1.05**	49.33	6.23	[55]
Case B	NACA 0012; $U_\infty = 56$; $c = 0.4$; $\alpha = 4\ ^o$; SS	19.61	1.43	137.00	**1.23**	[55]
Case C	NACA 0012; $U_\infty = 56$; $c = 0.4$; $\alpha = 4^o$; PS	22.83	2.30	43.64	**2.02**	[55]
Case D	DU-96-W-180; $U_e = 56$; $c = 0.3$; $\alpha = 4.6^o$; SS	**6.06**	62.49	87.10	13.31	[80]
Case E	DU-96-W-180; $U_e = 66$; $c = 0.3$; $\alpha = 10.3^o$; SS	54.26	313.74	217.38	**20.18**	[80]
Case F	NACA 0012; $U_\infty = 20$; $c = 0.2$; $\alpha = 0^o$	41.43	**5.39**	44.94	6.07	[15]
Case G	NACA 0018; $U_\infty = 20$; $c = 0.2$; $\alpha = 0^o$	60.18	16.79	113.86	**1.60**	[15]
Case H	NACA 63018; $U_\infty = 20$; $c = 0.2$; $\alpha = 0^o$	149.06	149.45	193.70	**14.70**	[15]
Average		43.44	66.39	111.41	**8.17**	
Maximum		149.06	294.92	221.08	**20.18**	
σ		46.14	105.52	68.53	**7.07**	

a linear decay in the high-frequency band, whose slope is discovered by the symbolic regression algorithm, as explained in Section 3.

Finally, the aerodynamic noise produced by a SWT-93-2.3 wind turbine is predicted and compared with field measurements reported in Christophe et al. [82]. Noise prediction assumes that turbulence interaction noise (also known as leading-edge noise) and trailing-edge noise are the unique noise sources of the wind turbine. For trailing-edge noise prediction, the model proposed in this research is used to calculate the WPS on both the suction and pressure sides. We compute wind turbine noise using the Amiet-Schlinker method for rotatory noise sources [83], where the relative motion of the segment that induces a delay between noise emission and the location of the observer is considered using the Doppler effect. The total noise of the wind turbine is calculated using the strip-theory approach, where the blade is divided into n segments that produce uncorrelated noise. Therefore, each segment is treated as a 2D airfoil, for which turbulence interaction noise and trailing-edge noise are computed using Amiet's theory [84,41]. Subsequently, the blade noise is calculated as the sum of all segments at every angular position. The total aerodynamic noise produced by the wind turbine is computed as the integral of the total blade noise at each azimuth angle over one rotation, considering a similar contribution of the three blades. A detailed description of the noise prediction approach is reported in [85,86].

The input for the prediction of turbulence interaction noise is the turbulence spectrum, which is computed with the von Kárman Spectrum, using as input the atmospheric turbulence intensity (Tu_∞) and atmospheric turbulent integral length scale (L). Predictions are computed with Tu_∞ =10.7%, and L =300 m, which are reported in the literature for this benchmark case [87]. For trailing-edge noise prediction, the inputs for Amiet's theory are the WPS, which is computed with the model proposed in this research, and the spanwise correlation length, which is computed using Corco's method Corcos [44]. To calculate the WPS, the inputs needed are the angle of attack and apparent velocity, which are used to perform XFOIL simulations to extract the boundary layer parameters (δ, δ^*, θ, and τ_w). The transition for XFOIL simulations was forced at x/c =0.05. An aerodynamic analysis of the wind turbine was performed using blade element momentum theory (BEMT) to obtain the angle of attack and apparent velocity distribution, i.e., the sum of the inflow velocity, rotational velocity, and induced velocity. BEMT calculations were performed using the open source code OpenFast, which includes the Prandtl tip and root loss correction factors and the Pitt / Peters skewed wake correction model [88].

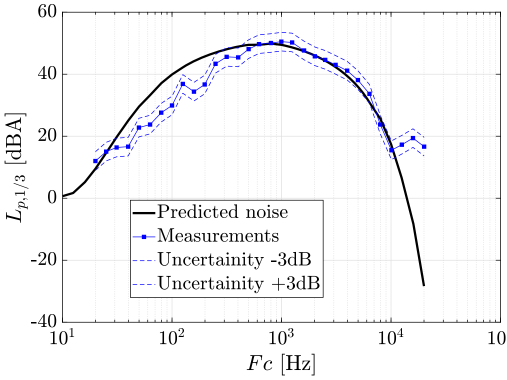

Fig. 9. Wind turbine noise prediction and measurements using the proposed WPS model.

The operating conditions of the wind turbine are: 17.5 rpm rotational speed, 9.5 m/s inflow velocity, and 5° collective pitch angle. The observer is located on the ground 100 m downstream of the wind turbine. The inner portion of the blade that is composed of cylinders is neglected. Table C.13 shows the geometrical characteristics along the blade (airfoil, chord, segment span, and twist angle), and the results from the BEMT simulations (angle of attack and apparent velocity). More information on turbine geometry and operational conditions can be found in Christophe et al. [82].

In this final validation, the WPS model is extrapolated to different airfoil geometries, inflow velocities, and angle of attack. There is a good agreement between the predicted noise and the measurements (see Fig. 9), mainly in the frequency range where trailing-edge noise is more relevant, i.e., f >0.7 kHz [85]. The results show once again the robustness of the model and its good performance for an extensive range of applications.

5. Conclusions

This paper presents a new empirical model to predict the WPS of turbulent boundary layers of mid to high Reynolds numbers under both adverse and favorable pressure gradients. The model is derived from experimental measurements of wall-pressure fluctuations on the suction and pressure sides of two airfoils across a wide range of inflow velocities and angles of attack. Unlike conventional single-equation models, the proposed model divides the WPS into three frequency bands, accounting for the physics of the turbulent scales that contribute to wall pressure fluctuations in different frequency ranges. Symbolic regression is used to derive mathematical expressions for each frequency range, using boundary layer parameters that can be obtained from simple tools such as XFOIL (or CFD simulations), thus preserving the simplicity and efficiency of single-equation models. The resulting model consists of five equations: three for the WPS levels in each frequency range and two for the boundary frequencies.

The model is validated against experimental data from the literature that encompass various airfoils, Reynolds numbers, and angles of attack. The results demonstrate the good performance of the model under a variety of conditions. Slightly reduction in accuracy is observed for strong adverse pressure gradients (pre-stall angles of attack), which is attributed to XFOIL predictions at high angles of attack. Overall, the model exhibits greater robustness compared to widely used semi-empirical and empirical alternatives, since it has the lowest maximum and average error and the lowest standard deviation for the validation cases. The standard deviation of our model is 7.07, compared to 46.1, 68.5, and 105.5 observed for other semiempirical methods. Finally, the model is challenged to predict full-scale wind turbine trailing-edge noise, achieving good agreement (within less than 1 dB) with field measurements.

While the proposed model offers clear improvements in simplicity and predictive robustness, several limitations warrant further investigation. First, its current formulation relies on XFOIL (or equivalent CFD) predictions of boundary layer parameters, which may introduce uncertainty under strong separation or three-dimensional flow effects. Second, model accuracy has not been thoroughly tested in highly unsteady or turbulent inflow conditions and may degrade outside the quasi-steady, two-dimensional regimes studied here. Furthermore, empirical methods will always be based on the database used. Future work should address these limitations to enhance the generality of the model, increasing the training data set where large-scale applications are considered, unsteady inflow, and experimental measurements of the boundary layer. This would allow the incorporation of fast turnaround methods in aerodynamic noise prediction and control.

CRediT authorship contribution statement

Laura Botero-Bolívar: Writing – original draft, Visualization, Validation, Software, Methodology, Investigation, Formal analysis, Data curation, Conceptualization. **David Huergo:** Writing – original draft, Validation, Methodology, Investigation, Formal analysis, Conceptualization. **Fernanda L. dos Santos:** Writing – review & editing, Investigation, Data curation. **Cornelis H. Venner:** Supervision, Resources, Project administration. **Leandro D. de Santana:** Supervision, Project administration, Funding acquisition. **Esteban Ferrer:** Writing – review & editing, Resources, Project administration, Funding acquisition.

Funding sources

This research has received funding from the European Union (ERC, Off-coustics, project number 101086075) and also from the European Commission through the H2020-MSCA-ITN-209 project zEPHYR (grant agreement No 860101). Views and opinions expressed are, however, those of the authors only and do not necessarily reflect those of the European Union or the European Research Council. Neither the European Union nor the granting authority can be held responsible for them. DH and EF acknowledge the funding received by the Comunidad de Madrid according to Orden 5067/2023, of December 27th, issued by the Consejero de Educación, Ciencia y Universidades, which announces grants for the hiring of predoctoral research personnel in training for the year 2023.

Declaration of competing interest

The authors declare the following financial interests/personal relationships which may be considered as potential competing interests: Laura Botero-Bolivar reports financial support was provided by European Union (grant agreement No 860101). Esteban Ferrer reports financial support was provided by European Union (project number 101086075). David Huergo reports financial support was provided by Community of Madrid (orden No 5067/2023). If there are other authors, they declare that they have no known competing financial interests or personal relationships that could have appeared to influence the work reported in this paper.

Acknowledgements

The authors would like to acknowledge Ing. W. Lette, ir. E. Leusink, S. Wanrooij for the technical support on the experimental setup and conduction of the experiments.

Appendix A. Remote microphone probes calibration

The calibration of the remote microphone probes consisted of obtaining a transfer function between an ideal microphone that is flushed-mounted with the airfoil surface and the remote microphone probe. For that, an in-house calibrator, shown in Fig. A.10 is used. The calibrator design is based on that presented by Roger [89]. It is equipped with a reference microphone, i.e., a GRAS 40HP, and an FR8 loudspeaker. The noise source was white noise. The calibration was done in situ when the airfoils were installed in the wind tunnel and consisted of two steps to minimize the influence of the calibrator in the calibration procedure [89,90]. The first step consisted in measuring the reference microphone (ref) in the calibrator and a microphone flush-mounted (FM), i.e., a GRAS 40HP, simultaneously. This results in the transfer function:

$$\mathrm{TF}_{\mathrm{ref,FM}} = \frac{\Phi_{\mathrm{ref,ref}}}{\Phi_{\mathrm{ref,FM}}}. \tag{A.1}$$

Then, a transfer function between the reference microphone in the calibrator and the remote microphone probe (RMP), i.e., a Knowles FG 23329-P07, was obtained:

$$\mathrm{TF}_{\mathrm{ref,RMP}} = \frac{\Phi_{\mathrm{ref,ref}}}{\Phi_{\mathrm{ref,RMP}}}. \tag{A.2}$$

The transfer function between the microphone flush-mounted and the remote microphone probe is the ratio of the two transfer functions:

$$|\mathrm{TF}_{\mathrm{FM,rmp}}|^2 = \frac{|\mathrm{TF}_{\mathrm{ref,RMP}}|^2}{|\mathrm{TF}_{\mathrm{ref,FM}}|^2}. \tag{A.3}$$

In Eqs. (A.1) to (A.3), $\Phi_{\mathrm{x,x}}$ and $\Phi_{\mathrm{x,y}}$ are the auto- and cross-spectrum of microphone signals represented by the subindex in the equations. The measurements of the RMP were corrected using the final transfer function, i.e., Eq. (A.3), to obtain the equivalent spectrum of the WPS at the airfoil surface (Φ_{pp}):

$$\Phi = \frac{\Phi_{\mathrm{rmp,rmp}}}{|TF_{\mathrm{FM,rmp}}|^2} \tag{A.4}$$

The coherence between the reference microphone in the calibrator and the remote microphone probe was analyzed to ensure that both

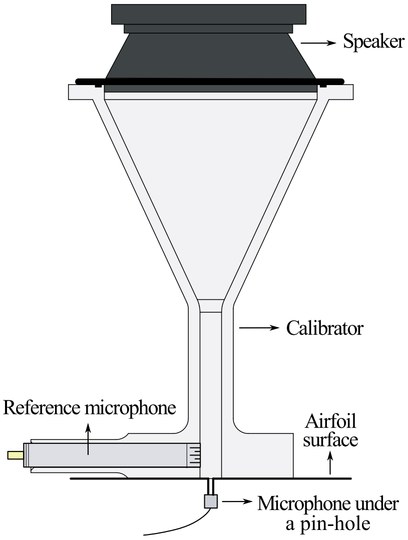

Fig. A.10. In-house calibrator.

microphones were in the same acoustic field. Due to contamination in the high-frequency range of electronic noise during the calibration, the spectrum is analyzed only up to a frequency of 5 kHz.

Appendix B. XFOIL simulations validation

XFOIL simulations were conducted to obtain the boundary layer parameters used in the symbolic regression approach to propose the model. The validation is performed by comparing the results with measurements of the boundary layer and pressure coefficient distribution. This appendix addresses the methodology of the measurements of the boundary layer and steady surface pressure and the comparison between experimental and XFOIL results.

B.1. Boundary layer measurements

Boundary layer measurements were performed at 97% of the airfoil chord on the suction side, using a Dantec Dynamics model 55P15 single-wire probe of 5 μm diameter and 1.25 mm wire length. The hot wire data were acquired with the Dantec StreamLine Pro CTA system coupled with a National Instruments 9215 A/D converter. Temperature correction was conducted for the measurements, adopting 21 °C as the reference temperature. Measurements were acquired during 20 s with a sampling frequency of 65536 (2^{16}) Hz. An anti-aliasing cutoff filter was used at a frequency of 30 kHz. Furthermore, a high-pass filter of 10 Hz was used during the processing of the data to eliminate the effects related to the flow buffeting instability that is naturally present in open wind tunnels in the test section [91]. The probe was mounted in a Dantec Dynamics 55H22 probe support installed on a symmetric airfoil, which was fixed in a 3D traverse system, allowing probe translation with a resolution of 6.5 μm.

The hot-wire calibration was performed in situ in the close test section with a Prandtl tube as a reference. The calibration consisted of 32 velocity points distributed logarithmically ranging from 2.5 to 50 m/s. The velocity measurements had a maximum system uncertainty of 5% with a confidence interval of 95%. This uncertainty was computed following the guidelines provided by Dantec Dynamics, which considers calibration equipment, calibration linearization, A/D board resolution, probe positioning, and temperature variations.

On average, velocity was measured at 35 locations across the boundary layer and five points in the free stream. The distribution of the measurements across the boundary layer was logarithmic. The distance of the probe to the wall was determined by the contact of a feeler gauge to the hot-wire prongs. The gauge accuracy is 0.05 mm. The distance from the wall of the first measurement varied from 0.5 mm to 1 mm among the configurations.

The experimental boundary layer displacement thickness (δ^*) and momentum thickness (θ) are determined by performing a trapezoidal numerical integration of the measured boundary layer velocity profile. The boundary layer thickness (δ) is determined according to Eq. (3), following the same approach as that used in the XFOIL simulations. The friction velocity is calculated by fitting the experimental mean velocity profile to the Prandtl-von Kármán log-law coupled with Coles' wake law:

$$\frac{U}{u_\tau} = \frac{1}{\kappa}\log\left(y^+\right) + B + \frac{2\Pi_w}{\kappa}\sin^2\left(\frac{\pi y}{2\delta}\right). \tag{B.1}$$

The fitting also determines the wake factor Π_w. The parameter κ denotes the von Kármán constant, equal to 0.38, B is a level constant equal to 5, and y^+ is the non-dimensional distance from the wall, defined as $y^+ = yu_\tau/\nu$.

B.2. Steady surface pressure measurements

The anechoic termination of the remote microphone probes located along the chord was connected to a NetScanner model 9216 pressure scanner to obtain the static pressure on the airfoil surface. Therefore, the unsteady and steady surface pressure were measured simultaneously. Twenty sensors are located on the suction and pressure sides distributed along the chord. Measurements were taken during 30 s with a sampling frequency of 300 Hz. The pressure coefficient, C_p, is calculated according to:

$$C_\mathrm{p} = \frac{p - P_\infty}{\frac{1}{2}\rho U^2}, \tag{B.2}$$

where ρ is the air density, and U is the inflow velocity, which is measured by a Prandtl tube located at the end of the close test section.

B.3. XFOIL validation with experimental data

Fig. B.11 shows the comparison of the pressure coefficient (Cp) distribution obtained experimentally and with XFOIL for $U = 30$ m/s at different effective angles of attack for both airfoils. A good agreement is obtained in all the cases for both, suction and pressure sides. XFOIL captures well the suction peak and the pressure gradient along the chord. A small deviation is obtained between $x/c = 0.065$ and 0.1 because those pressure ports were located right before and after the tripping device, which disturbs the mean flow.

Tables B.5 to B.12 show the comparison between experimental measurements and XFOIL simulations of δ^*, and θ and calculated u_τ and δ. There is a good agreement between the XFOIL results and the experimental data for airfoils and all conditions. XFOIL follows the same trend as the experimental results with the velocity and angle of attack, such as δ increasing with the angle of attack and decreasing with the inflow velocity, while u_τ decreasing with the angle of attack. The highest error appears for higher angles of attack and lower velocities. However, the errors are acceptable considering the many factors that can influence the boundary layer measured, such as the determination of the distance from the wall and the tripping device and transition process, which are more critical for lower Reynolds numbers. In general, using XFOIL to estimate boundary layer parameters is reasonable to propose the WPS model, given that it is a common methodology to predict WPS and trailing-edge noise [92–94].

Appendix C. Wind turbine blade geometry

Table C.13 shows the distribution along the radius (r) of the geometrical parameters of the segments of the SWT-2.3-93 wind turbine blade for the noise prediction, i.e. airfoil, chord (c), span (b), twist angle (β) and the results of the BEMT calculations, i.e., apparent velocity (U_app), and angle of attack (α).

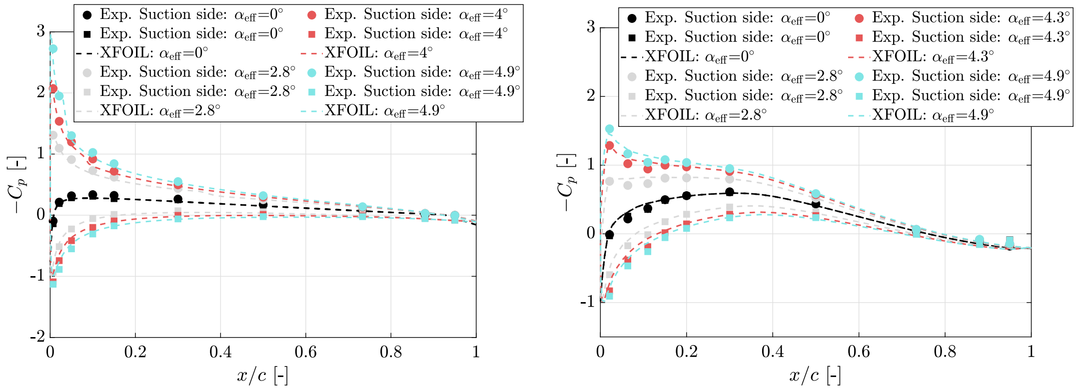

(a) NACA 0008 (b) NACA 63018

Fig. B.11. Pressure coefficient distribution compared with XFOIL results for several angles of attack. $U = 30$ m/s. $Re = 600 \times 10^3$.

Table B.5
Comparison between XFOIL and experimental measurements of δ^* on the suction side for different angles of attack for the NACA 0008 airfoil. The values between curly brackets correspond to the boundary layer parameters for $\alpha_{\text{eff}} = \{0°, 3°, 5°\}$.

U [m/s]	δ^* [mm]		
	Exp.	XFOIL	$\frac{\lvert \text{Exp.}-\text{XFOIL}\rvert}{\text{Exp.}}$
10	{1.5, 2.3, 4.0}	{1.9, 2.5, 3.3}	{26.6%, 8.7%, 17.5%}
30	{1.1, 1.8, 2.8}	{1.4, 1.9, 2.4}	{27.7%, 5.5%, 14.3%}
45	{-, 1.7, 2.5}	{-, 1.7, 2.2}	{0.5%, 12.0%}

Table B.6
Comparison between XFOIL and experimental measurements of θ^* on the suction side for different angles of attack for the NACA 0008 airfoil. The values between curly brackets correspond to the boundary layer parameters for $\alpha_{\text{eff}} = \{0°, 3°, 5°\}$.

U [m/s]	θ^* [mm]		
	Exp.	XFOIL	$\frac{\lvert \text{Exp.}-\text{XFOIL}\rvert}{\text{Exp.}}$
10	{1.1, 1.4, 2.1}	{1.2, 1.5, 1.9}	{9.1%, 7.1%, 9.5%}
30	{0.8, 1.2, 1.6}	{0.9, 1.2 1.5}	{12.5%, 0.5%, 6.2%}
45	{-, 1.1 1.6}	{-, 1.1, 1.4}	{0.3%, 12.5%}

Table B.7
Comparison between XFOIL and experimental measurements of u_τ on the suction side for different angles of attack for the NACA 0008 airfoil. The values between curly brackets correspond to the boundary layer parameters for $\alpha_{\text{eff}} = \{0°, 3°, 5°\}$.

U [m/s]	u_τ [m/s]		
	Exp.	XFOIL	$\frac{\lvert \text{Exp.}-\text{XFOIL}\rvert}{\text{Exp.}}$
10	{0.37, 0.29, 0.17}	{0.39, 0.36, 0.33}	{-, 5.4%, 24.1%, 9.41%}
30	{1.08, 0.88, 0.62}	{1.1, 1.02, 0.68}	{-, 1.9%, 15.9%, 9.7%}
45	{-, 1.31, 1.34}	{-, 1.5, 1.39}	{-, 14.5%, 3.7%}

Table B.8
Comparison between XFOIL and experimental measurements of δ on the suction side for different angles of attack for the NACA 0008 airfoil. The values between curly brackets correspond to the boundary layer parameters for $\alpha_{\text{eff}} = \{0°, 3°, 5°\}$.

U [m/s]	δ [mm]		
	Exp.	XFOIL	$\frac{\lvert \text{Exp.}-\text{XFOIL}\rvert}{\text{Exp.}}$
10	{8.9, 11.3, 14.7}	{9.2, 11.4, 14.3}	{-, 3.3%, 0.9%, 2.7%}
30	{7.0, 9.3, 12.1}	{7.4, 9.1, 11.4}	{-, 5.7%, 2.1%, 5.8%}
45	{-, 9.6, 12.7}	{-, 8.4, 10.5}	{-, 12.5%, 17.3%}

Table B.9
Comparison between XFOIL and experimental measurements of δ^* on the suction side for different angles of attack for the NACA 63018 airfoil. The values between curly brackets correspond to the boundary layer parameters for $\alpha_{\text{eff}} = \{0°, 3°\}$.

U [m/s]	δ^* [mm]		
	Exp.	XFOIL	$\frac{\lvert \text{Exp.}-\text{XFOIL}\rvert}{\text{Exp.}}$
10	{3.3, 3.7}	{3.4, 4.7}	{3.0%, 27.0%}
30	{2.0, 2.1}	{2.5, 3.4}	{25.0%, 61.9%}

Table B.10
Comparison between XFOIL and experimental measurements of θ^* on the suction side for different angles of attack for the NACA 63018 airfoil. The values between curly brackets correspond to the boundary layer parameters for $\alpha_{\text{eff}} = \{0°, 3°\}$.

U [m/s]	θ^* [mm]		
	Exp.	XFOIL	$\frac{\lvert \text{Exp.}-\text{XFOIL}\rvert}{\text{Exp.}}$
10	{1.6, 1.7}	{1.8, 2.2}	{12.5%, 29.4%}
30	{1.3, 1.4}	{1.5, 1.8}	{15.4%, 28.5%}

Table B.11
Comparison between XFOIL and experimental measurements of u_τ on the suction side for different angles of attack for the NACA 63018 airfoil. The values between curly brackets correspond to the boundary layer parameters for $\alpha_{\text{eff}} = \{0°, 3°\}$.

U [m/s]	u_τ [m/s]		
	Exp.	XFOIL	$\frac{\lvert \text{Exp.}-\text{XFOIL}\rvert}{\text{Exp.}}$
10	{0.22, 0.14}	{0.28, 0.22}	{27.3%, 57.1%}
30	{0.83, 0.64}	{0.81, 0.68}	{2.4%, 6.3%}

Table B.12
Comparison between XFOIL and experimental measurements of δ on the suction side for different angles of attack for the NACA 63018 airfoil. The values between curly brackets correspond to the boundary layer parameters for $\alpha_{\text{eff}} = \{0°, 3°\}$.

U [m/s]	δ [mm]		
	Exp.	XFOIL	$\frac{\lvert \text{Exp.}-\text{XFOIL}\rvert}{\text{Exp.}}$
10	{10.2, 12.0}	{11.3, 15.4}	{10.8%, 28.3%}
30	{8.8, 9.5}	{10.5, 12.5}	{19.3%, 31.6%}

Table C.13
Distribution of the conditions for the WPS prediction of the SWT-2.3-93 wind turbine.

Airfoil	r [m]	β [deg.]	c [m]	b [m]	U_{app} [m/s]	$Re/10^6$ [-]	α [°]
FFA-W3-301	14.2	10	3.4	10.4	26.7	6.1	0.28
FFA-W3-241	23.4	5.7	2.7	8.1	42.5	7.5	-1.10
NACA 63-221	30.5	1.2	2.0	6.2	55.0	7.5	0.22
NACA 63-218	36.0	-0.6	1.6	4.7	64.6	6.7	1.12
NACA 63-218	40.0	1.4	1.2	3.6	71.9	5.7	1.70
NACA 63-218	43.3	-1.8	0.9	2.8	77.6	4.7	2.10
NACA 63-218	45.6	-1.8	0.7	1.8	81.7	3.6	2.20

Data availability

Data will be made available on request.

References

[1] Abrahamsen K. The ship as an underwater noise source. Proc Meet Acoust 2012;17:1. https://doi.org/10.1121/1.4772953.

[2] Kurt RE, Khalid H, Turan O, Houben M, Bos J, Helvacioglu IH. Towards human-oriented norms: considering the effects of noise exposure on board ships. Ocean Eng 2016;120:101–7. https://doi.org/10.1016/j.oceaneng.2016.03.049.

[3] Götz T, Hastie G, Hatch L, Raustein O, Southall B, Tasker M, et al. Overview of the impacts of anthropogenic underwater sound in the marine environment. Technical Report. OSPAR Commission; 2009.

[4] Erbe C, Thomas JA. Exploring animal behavior through sound: volume. Switzerland: Springer Nature Gewerbestrasse; 2022.

[5] European Parliament. Directive 2002/49/EC of the European Parliament and of the Council of 25 June 2002 relating to the assessment and management of environmental noise. Off J Eur Communities 2002.

[6] ICAO. Environmental report 2016, Aviation and climate change 2016; 2016.

[7] Baudin E, Mumm H. Guidelines for regulation on UW noise from commercial shipping. Technical Report Deliverable 5.4. Bureau Veritas, DNV GL; 2015.

[8] Davy JL, Burgemeister K, Hillman D. Wind turbine sound limits: current status and recommendations based on mitigating noise annoyance. Appl Acoust 2018;140:288–95. https://doi.org/10.1016/j.apacoust.2018.06.009.

[9] Roger M, Moreau S. Back-scattering correction and further extensions of Amiet's trailing-edge noise model. Part 1: theory. J Sound Vib 2005;286:477–506. https://doi.org/10.1016/j.jsv.2004.10.054.

[10] Moreau S, Roger M. Effect of airfoil aerodynamic loading on trailing edge noise sources. AIAA J 2005;43:41–52. https://doi.org/10.2514/1.5578.

[11] Shannon D, Morris S, Mueller T. Trailing edge flow physics and acoustics. In: 11th AIAA/CEAS aeroacoustics conference; 2005. p. 2957.

[12] Garcia-Sagrado A, Hynes T, Hodson H. Experimental investigation into trailing edge noise sources. In: 12th AIAA/CEAS aeroacoustics conference (27th AIAA aeroacoustics conference); 2006. p. 2476.

[13] Shannon D, Morris SC. Trailing edge noise measurements using a large aperture phased array. Int J Aeroacoust 2008;7:147–76. https://doi.org/10.1260/147547208784649446.

[14] dos Santos FL, Even NA, Botero-Bolivar L, Venner CH, de Santana LD. Influence of surface roughness geometry on trailing edge wall pressure fluctuations and noise. In: AIAA aviation 2021 forum; 2021.

[15] Sanders M, Koenjer C, Botero-Bolívar L, dos Santos F, Venner C, de Santana L. Trailing-edge noise comparability in open, closed, and hybrid wind tunnel test sections. AIAA J 2022:1–15. https://doi.org/10.2514/1.J061460.

[16] dos Santos FL, Botero-Bolívar L, Venner CH, de Santana LD. Wall-pressure spectra, spanwise correlation, and far-field noise measurements of a naca 0008 airfoil under uniform and turbulent inflows. Appl Acoust 2023;211:109546. https://doi.org/10.1016/j.apacoust.2023.109546.

[17] Botero-Bolívar L, dos Santos FL, Venner CH, de Santana LD. Experimental and predicted leading- and trailing-edge noise of symmetric airfoils under zero mean-loading. Appl Acoust 2023;212:1–14. https://doi.org/10.1016/j.apacoust.2023.109579.

[18] Botero-Bolívar L, dos Santos FL, Venner CH, de Santana LD. Trailing-edge far-field noise and noise source characterization in high inflow turbulence conditions. J Acoust Soc Am 2024;155:803–16. https://doi.org/10.1121/10.0024611.

[19] Sandberg RD, Sandham ND. Direct numerical simulation of turbulent flow past a trailing edge and the associated noise generation. J Fluid Mech 2008;596:353–85. https://doi.org/10.1017/S0022112007009561.

[20] Oberai AA, Roknaldin F, Hughes TJ. Computation of trailing-edge noise due to turbulent flow over an airfoil. AIAA J 2002;40:2206–16. https://doi.org/10.2514/2.1582.

[21] Winkler J, Moreau S, Carolus T. Large-eddy simulation and trailing-edge noise prediction of an airfoil with boundary-layer tripping. In: 15th AIAA/CEAS aeroacoustics conference (30th AIAA aeroacoustics conference); 2009. p. 3197.

[22] Wolf WR, Lele SK. Trailing-edge noise predictions using compressible large-eddy simulation and acoustic analogy. AIAA J 2012;50:2423–34. https://doi.org/10.2514/1.J051638.

[23] Winkler J, Wu H, Moreau S, Carolus T, Sandberg RD. Trailing-edge broadband noise prediction of an airfoil with boundary-layer tripping. J Sound Vib 2020;482:115450. https://doi.org/10.1016/j.jsv.2020.115450.

[24] Howe M. A review of the theory of trailing edge noise. J Sound Vib 1978;61:437–65. https://doi.org/10.1016/0022-460X(78)90391-7.

[25] Doolan CJ, Moreau DJ. A review of airfoil trailing edge noise with some implications for wind turbines. Int J Aeroacoust 2015;14:811–32. https://doi.org/10.1260/1475-472X.14.5-6.811.

[26] Lee S, Ayton L, Bertagnolio F, Moreau S, Chong TP, Joseph P. Turbulent boundary layer trailing-edge noise: theory, computation, experiment, and application. Prog Aerosp Sci 2021;126:100737. https://doi.org/10.1016/j.paerosci.2021.100737.

[27] Howe M. Aerodynamic noise of a serrated trailing edge. J Fluids Struct 1991;5:33–45. https://doi.org/10.1016/0889-9746(91)80010-B.

[28] Lyu B, Azarpeyvand M, Sinayoko S. Prediction of noise from serrated trailing edges. J Fluid Mech 2016;793:556–88. https://doi.org/10.1017/jfm.2016.132.

[29] Moreau S, Sanjosé M, Lyu B, Ayton LJ. Analytical, numerical and experimental investigation of trailing-edge noise reduction on a controlled diffusion airfoil with serrations. In: 25th AIAA/CEAS aeroacoustics conference; 2019. p. 2450.

[30] Pereira LTL, Avallone F, Ragni D, Scarano F. A parametric study of serration design for trailing–edge broadband noise reduction. Appl Acoust 2023;211:109470. https://doi.org/10.1016/j.apacoust.2023.109470.

[31] Oerlemans S. Reduction of wind turbine noise using blade trailing edge devices. In: 22nd AIAA/CEAS aeroacoustics conference; 2016. p. 3018.

[32] Rossignol K-S, Suryadi A, Herr M, Schmidt J, Tychsen J. Experimental investigation of porous materials for trailing-edge noise reduction. Int J Aeroacoust 2020;19:365–84. https://doi.org/10.1177/1475472X20954421.

[33] Ali SAS, Azarpeyvand M, Da Silva CRI. Trailing-edge flow and noise control using porous treatments. J Fluid Mech 2018;850:83–119. https://doi.org/10.1017/jfm.2018.430.

[34] Zhang M, Chong TP. Experimental investigation of the impact of porous parameters on trailing-edge noise. J Sound Vib 2020;489:115694. https://doi.org/10.1016/j.jsv.2020.115694.

[35] Geyer T, Sarradj E, Fritzsche C. Measurement of the noise generation at the trailing edge of porous airfoils. Exp Fluids 2010;48:291–308. https://doi.org/10.1007/s00348-009-0739-x.

[36] Gruber M. Airfoil noise reduction by edge treatments. Ph.D. thesis. University of Southampton; 2012.

[37] Powell A. On the aerodynamic noise of a rigid flat plate moving at zero incidence. J Acoust Soc Am 1959;31:1649–53. https://doi.org/10.1121/1.1907674. https://pubs.aip.org/asa/jasa/article-pdf/31/12/1649/18740303/1649_1_online.pdf.

[38] Ffowcs Williams JE, Hall L. Aerodynamic sound generation by turbulent flow in the vicinity of a scattering half plane. J Fluid Mech 1970;40:657–70. https://doi.org/10.1017/S0022112070000368.

[39] Blake WK, Gershfeld JL. The aeroacoustics of trailing edges. Springer Berlin Heidelberg; 1989.

[40] Brooks T, Hodgson T. Trailing edge noise prediction from measured surface pressures. J Sound Vib 1981;78:69–117. https://doi.org/10.1016/S0022-460X(81)80158-7.

[41] Amiet RK. Noise due to turbulent flow past a trailing edge. J Sound Vib 1976;47:387–93. https://doi.org/10.1016/0022-460X(76)90948-2.

[42] Glegg S, Devenport W. Aeroacoustics of low Mach number flows. Academic Press; 2017.

[43] Goody M. Empirical spectral model of surface pressure fluctuations. AIAA J 2004;42:1788–94. https://doi.org/10.2514/1.9433.

[44] Corcos G. The structure of the turbulent pressure field in boundary-layer flows. J Fluid Mech 1964;18:353–78. https://doi.org/10.1017/S002211206400026X. cited by: 556.

[45] Chase DM. Modeling the wavevector-frequency spectrum of turbulent boundary layer wall pressure. J Sound Vib 1980;70:29–67. https://doi.org/10.1016/0022-460X(80)90553-2.

[46] Catlett MR, Anderson JM, Forest JB, Stewart DO. Empirical modeling of pressure spectra in adverse pressure gradient turbulent boundary layers. AIAA J 2016;54:569–87. https://doi.org/10.2514/1.J054375.

[47] Rozenberg Y, Robert G, Moreau S. Wall-pressure spectral model including the adverse pressure gradient effects. AIAA J 2012;50:2168–79. https://doi.org/10.2514/1.J051500.

[48] Kamruzzaman M, Bekiropoulos D, Lutz T, Würz W, Krämer E. A semi-empirical surface pressure spectrum model for airfoil trailing-edge noise prediction. Int J Aeroacoust 2015;14:833–82. https://doi.org/10.1260/1475-472X.14.5-6.833.

[49] Hu N, Herr M. Characteristics of wall pressure fluctuations for a flat plate turbulent boundary layer with pressure gradients. In: 22nd AIAA/CEAS aeroacoustics conference; 2016. p. 2749.

[50] Parchen RR. Progress report DRAW: a prediction scheme for trailing edge noise based on detailed boundary layer characteristics. TNO Institute of Applied Physics; 1998.

[51] Lee S. Empirical wall-pressure spectral modeling for zero and adverse pressure gradient flows. AIAA J 2018;56:1818–29. https://doi.org/10.2514/1.J056528.

[52] Pargal S, Yuan J, Moreau S. Wall-pressure spectra under turbulent boundary layers with equilibrium pressure gradients. In: 30th AIAA/CEAS aeroacoustics conference; 2024. p. 3393.

[53] Dominique J, Van den Berghe J, Schram C, Mendez MA. Artificial neural networks modeling of wall pressure spectra beneath turbulent boundary layers. Phys Fluids 2022;34:035119. https://doi.org/10.1063/5.0083241.

[54] Arroyo Ramo A, Alguacil A, Bauerheim M, Moreau S, Jacob MC. Artificial neural networks prediction of wall-pressure spectrum. In: 30th AIAA/CEAS aeroacoustics conference; 2024. p. 3140.

[55] Küçükosman YC, Christophe J, Schram C. Trailing edge noise prediction based on wall pressure spectrum models for naca0012 airfoil. J Wind Eng Ind Aerodyn 2018;175:305–16.

[56] Kissner CA, Guerin S, Bianchi S, Node-Langlois T. On the modeling of wall surface pressure spectra for trailing edge noise prediction. In: 28th AIAA/CEAS aeroacoustics 2022 conference; 2022. p. 2800.

[57] Fritsch DJ, Vishwanathan V, Roy CJ, Todd Lowe K, Devenport WJ, Croaker P, et al. Modeling the surface pressure spectrum beneath turbulent boundary layers in pressure gradients. AIAA J 2023;61.

[58] Drela M. Xfoil: an analysis and design system for low Reynolds number airfoils. Springer; 1989. p. 1–12.

[59] Tenachi W, Ibata R, Diakogiannis FI. Deep symbolic regression for physics guided by units constraints: toward the automated discovery of physical laws. Astrophys J 2023;959:99.

[60] Wang D, Chen Y, Chen S. Discovering an interpretable mathematical expression for a full wind-turbine wake with artificial intelligence enhanced symbolic regression. Phys Fluids 2024;36.

[61] Vaddireddy H, Rasheed A, Staples AE, San O. Feature engineering and symbolic regression methods for detecting hidden physics from sparse sensor observation data. Phys Fluids 2020;32.

[62] Lozano-Durán A, Bassenne M. Towards model discovery with reinforcement learning. Annu Res Briefs 2019.

[63] Wang Y, Wagner N, Rondinelli JM. Symbolic regression in materials science. MRS Commun 2019;9:793–805.

[64] Quade M, Abel M, Shafi K, Niven RK, Noack BR. Prediction of dynamical systems by symbolic regression. Phys Rev E 2016;94:012214.

[65] Tohme T, Khojasteh MJ, Sadr M, Meyer F, Youcef-Toumi K. Isr: invertible symbolic regression. arXiv preprint. arXiv:2405.06848, 2024.

[66] Sarradj E, Geyer T. Symbolic regression modeling of noise generation at porous airfoils. J Sound Vib 2014;333:3189–202.

[67] Gill H, Lee S. Development of new empirical rotor broadband noise prediction models for urban air mobility applications. In: AIAA SCITECH 2024 forum; 2024. p. 2473.

[68] Shubham S, Pargal S, Moreau S, Sandberg RD, Yuan J, Kushari A, et al. Data-driven empirical wall pressure spectrum models for fan noise prediction. In: AIAA aviation 2023 forum; 2023. p. 3508.

[69] Dominique J, Christophe J, Schram C, Sandberg RD. Inferring empirical wall pressure spectral models with gene expression programming. J Sound Vib 2021;506:116162.

[70] Kurhade NN, Vadlamani NR, Haridas A. Artificial neural networks and guided gene expression programming to predict wall pressure spectra beneath turbulent boundary layers. Phys Fluids 2023;35.

[71] Cranmer M. Interpretable machine learning for science with pysr and symbolicregression.jl. arXiv preprint. arXiv:2305.01582, 2023.

[72] Brindle A. Genetic algorithms for function optimization. Ph.D. thesis. University of Alberta; 1980.

[73] Kirkpatrick S, Gelatt Jr CD, Vecchi MP. Optimization by simulated annealing. Science 1983;220:671–80.

[74] Broyden CG. The convergence of a class of double-rank minimization algorithms 1. General considerations. IMA J Appl Math 1970;6:76–90.

[75] de Santana LD, Sanders MP, Venner CH, Hoeijmakers HW. The utwente aeroacoustic wind tunnel upgrade. In: 24th AIAA/CEAS aeroacoustics conference; 2018. p. 3136.

[76] Brooks TF, Pope DS, Marcolini MA. Airfoil self-noise and prediction. NASA; 1989.

[77] dos Santos FL, Botero-Bolívar L, Venner CH, de Santana LD. Analysis of the remote microphone probe technique for the determination of turbulence quantities. Appl Acoust 2023;208:109387. https://doi.org/10.1016/j.apacoust.2023.109387.

[78] Blake WK. Mechanics of flow-induced sound and vibration, volume 2: complex flow-structure interactions. Academic Press; 2017.

[79] Lee S, Villaescusa A. Comparison and assessment of recent empirical models for turbulent boundary layer wall pressure spectrum. In: 23rd AIAA/CEAS aeroacoustics conference; 2017. p. 3688.

[80] Suryadi A, Herr M. Wall pressure spectra on a du96-w-180 profile from low to pre-stall angles of attack. In: 21st AIAA/CEAS aeroacoustics conference; 2015. p. 2688.

[81] Botero-Bolívar L, dos Santos FL, Venner CH, de Santana LD. Study of the development of a boundary layer using the remote microphone probe technique. Exp Fluids 2023;64:88. https://doi.org/10.1007/s00348-023-03630-x.

[82] Christophe J, Buckingham S, Schram C, Oerlemans S. zephyr - large on shore wind turbine benchmark. Zenodo; 2022.

[83] Schlinker R, Amiet R. Helicopter rotor trailing edge noise. In: 7th aeroacoustics conference; 1981. p. 2001.

[84] Amiet RK. Acoustic radiation from an airfoil in a turbulent stream. J Sound Vib 1975;41:407–20. https://doi.org/10.1016/S0022-460X(75)80105-2.

[85] Botero-Bolívar L, Marino OA, Venner CH, de Santana LD, Ferrer E. Low-cost wind turbine aeroacoustic predictions using actuator lines. Renew Energy 2024;227:120476. https://doi.org/10.1016/j.renene.2024.120476.

[86] Botero-Bolívar L. Wind turbine noise prediction. https://github.com/lauraboterob/WindTurbineNoiseprediction. https://doi.org/10.5281/zenodo.8325974, 2023.

[87] Kale B. ABL simulations with uncertain weather parameters and impact on WT performance and near-field noise. Ph.D. thesis. Universidad Politécnica de Madrid; 2023.

[88] Bortolotti P, Masciola M, Ananthan S, Schmidt MJ, Rood J, Mendoza N, et al. Openfast. https://doi.org/10.5281/zenodo.6324288, 2022.

[89] Roger M. Microphone measurements in aeroacoustic installations. Educational notes, STO-EN-AVT-287. S&T Organization; 2017.

[90] Berntsen CR. The remote microphone probe for unsteady surface pressure measurement. Ph.D. thesis. University of Notre Dame; 2014.

[91] von Heesen W, Höpfer M. Suppression of wind tunnel buffeting by active flow control. In: SAE 2004 world congress & exhibition; 2004.

[92] Stalnov O, Chaitanya P, Joseph PF. Towards a non-empirical trailing edge noise prediction model. J Sound Vib 2016;372:50–68. https://doi.org/10.1016/j.jsv.2015.10.011.

[93] Lee S. The effect of airfoil shape on trailing edge noise. J Theor Comput Acoust 2019;27:1850020. https://doi.org/10.1142/S2591728518500202.

[94] Bertagnolio F, Madsen HA, Bak C. Trailing edge noise model validation and application to airfoil optimization. J Sol Energy Eng 2010;132:031010. https://doi.org/10.1115/1.4001462.